A systematic study on the influence of scale, hull roughness, and draft on form factor estimation

Citation for the original published paper (version of record):

Argyros, M., Mancini, S., Korkmaz, K. et al (2026). A systematic study on the influence of scale, hull roughness, and draft on form factor
estimation. International Journal of Naval Architecture and Ocean Engineering, 18.
http://dx.doi.org/10.1016/j.ijnaoe.2025.100739

International Journal of Naval Architecture and Ocean Engineering 18 (2026) 100739

Contents lists available at ScienceDirect

International Journal of Naval Architecture and Ocean Engineering

journal homepage: www.journals.elsevier.com/international-journal-of-naval-architecture-and-ocean-engineering/

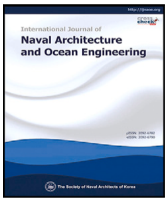

A systematic study on the influence of scale, hull roughness, and draft on form factor estimation

Minas Argyros [a], Simone Mancini [a,b,*], Kadir Burak Korkmaz [c], Arash Eslamdoost [d]

[a] *Department of Hydro and Aerodynamics, FORCE Technology, Hjortekærsvej 99, Kgs. Lyngby, Denmark*
[b] *Department of Industrial Engineering, University of Naples Federico II, Via Claudio 21, Napoli NA, Italy*
[c] *RISE Research Institutes of Sweden, Chalmers Tvärgata 10, Göteborg, Sweden*
[d] *Department of Mechanics and Maritime Sciences, Chalmers University of Technology, Chalmersplatsen 4, Gothenburg, Sweden*

ARTICLE INFO

Keywords:
Computational fluid dynamics
Scale effects
Roughness analysis
Form factor
2-*k* method
Benchmark hulls

ABSTRACT

In recent years, considerable attention has been given to the prediction of form factor of ships and the associated scale effects, as the accuracy of such estimations has come under scrutiny. This paper explores the discrepancies between model-scale and full-scale form factor predictions derived from CFD simulations using a newly developed approach known as the *2-k* method. This method enhances the precision of form factor evaluation, particularly when applied at full scale, showing notable improvements for hulls with wetted transoms. This study tests the hypothesis of 2-k and transom correction methods with different numerical tools and methods. It reveals a strong dependence of the form factor on grid resolution across different scales, while aligning well with findings reported in the literature. Additionally, a sensitivity analysis based on uniformly distributed surface roughness is performed. The *2-k* method is also applied to systematically varied transom submergence conditions, demonstrating consistent form factor trends across both model and full scales. Furthermore, when evaluating draft variations, the method yields results that more closely match experimental data. These findings suggest that the *2-k* method is a reliable tool for estimating the form factor in scenarios involving complex turbulent flow, such as in the wake of the transom.

1. Introduction

The accurate prediction of ship resistance is a cornerstone of naval architectural design, directly influencing propulsion power requirements and, ultimately, fuel efficiency and operational costs. Among the various components of total resistance, the viscous resistance, particularly the form factor $(1 + k)$, plays a critical role in capturing the influence of hull shape on viscous flow beyond simple frictional effects. Despite its widespread use in empirical methods such as the Prohaska method and its integration in ITTC procedures, the determination of form factor remains subject to uncertainties due to scale effects, flow separation, and geometric complexity.

In accordance with established practices and extensive knowledge, towing tank testing remains a fundamental method for evaluating a ship's performance. Hydrodynamic tests involve scaled model versions of actual vessels and are conducted in towing tanks. This traditional testing approach has led to the acquisition of extensive experience and knowledge in ship hydrodynamics, including databases of ship models, measurements, and statistical data. With the accumulation of invaluable information on ship hydrodynamics, standardized procedures have been devised to perform towing tank tests. The main responsible for organizing and publishing these procedures is the International Towing Tank Conference (ITTC).

Towing tank experiments are a traditional method for estimating ship resistance, yet they exhibit several limitations. A prominent issue lies in the disparity of viscous effects between model-scale and full-scale conditions. To address this, extrapolation techniques have been developed, which decompose the total resistance into its individual components and apply appropriate scaling to each. These methods aim to enhance the accuracy of full-scale performance predictions. Alternatively, computational fluid dynamics (CFD) has emerged as a powerful tool for resistance assessment by numerically solving the governing flow equations. With advancements in computational resources, CFD has become increasingly accessible to naval architects and designers.

It is a fact that CFD provides advantages, but it also conceals drawbacks. The main advantage of CFD is its ability to run full-scale simulations, which reduces uncertainties in the extrapolation from model to full-scale. Additionally, valuable flow information can be obtained from a CFD simulation, making it a viable positive choice.

---

[*] Corresponding author.
E-mail address: simone.mancini@unina.it (S. Mancini).

https://doi.org/10.1016/j.ijnaoe.2025.100739
Received 23 September 2025; Received in revised form 10 December 2025; Accepted 26 December 2025

Nomenclature

Greek symbols

α	Phase volume fraction
$\delta_{i,j}$	Kronecker delta
ϵ	Dissipation rate (m^2/s^3)
ϵ	Refinement ratio
μ	Dynamic viscosity ($N\ s/m^2$)
μ_t	Eddy viscosity ($N\ s/m^2$)
ν	Kinematic viscosity
ω	Specific turbulence dissipation rate (s^{-1})
Φ	Steady potential
ϕ	Extrapolated asymptotic value
ρ	Fluid density (kg/m^3)
σ	Viscous stresses (N/m^2)
θ	Velocity scale

Alphabetical symbols

$1+k$	Form factor
A_{max}	Maximum cross-section area for a given draft (m^2)
A_{tr}	Area of the submerged transom (m^2)
B	Beam of ship (m)
C_μ	Non-dimensional constant
C_A	Correlation coefficient
C_B	Block coefficient
C_F	Frictional resistance coefficient
C_{PV}	Viscous pressure resistance coefficient
C_T	Total resistance coefficient)
C_T	Total resistance coefficient
C_W	Wave resistance coefficient
e_a	Approximate error
e_{ext}	Extrapolated error
F_i	Force component (N)
Fr	Froude number
g	Gravitational acceleration (m/s^2)
k_e	Turbulence kinetic energy (m^2/s^2)
k_{tr}	Form factor of transom
l	Length scale
L_{PP}	Length between perpendiculars (m)
L_{WL}	Waterline length of ship (m)
n	Number of cells
p	Observed order of grid convergence
p	Pressure (Pa)
R^+	Roughness parameter
Re	Reynolds number
$S_{i,j}$	Rate of strain tensor
t	Time (s)
T_M	Amidships draft (m)
T_B	Ballast draft (m)
T_D	Design draft (m)
T_S	Scantling draft (m)
$tr_{fullness}$	Fullness of wetted-transom
tr_{ratio}	Area ratio of wetted-transom
U_G	Discretization uncertainty
U_I	Iterative uncertainty
U_r	"Imaginary" force used for water–air fraction in VoF method (N)
U_{SN}	Numerical uncertainty
V	Speed (m^2)
y	Distance to wall (m)
y^+	Non-dimensional wall distance
y_{tr}	Transverse dimension of wetted-transom (m)

Subscripts

d	Disturbed waves
I	Incident waves
i	Abscissa
j	Ordinate
M	Model-scale
S	Ship scale

Acronyms

2–k	Two form factor method
AHR	Average Hull Roughness
DFBI	Dynamic Fluid Body Interaction
EFD	Experimental Fluid Dynamics
F-S	Free-Surface Model
GCI	Grid Convergence Index
HRIC	High-Resolution Interface Capturing
ITTC	International Towing Tank Conference
RANS	Reynolds-Averaged Navier–Stokes
SST	Shear Stress Transport
V&V	Verification and Validation
VoF	Volume of Fluid

However, it should be noted that the CFD is affected by uncertainties and modeling errors. These errors occur because flow physics is simulated by using simplified models, such as the use of wall functions to represent turbulence effects inside the boundary layer (Mikkelsen et al., 2019) or the lack of accurate models to represent surface roughness.

In addition to the experimental methods for the determination of the form factor, such as Hughes (1954) and Prohaska (1966) methods, recently research studies have presented that a combination of CFD computations and Experimental Fluid Dynamics (EFD) can handle scale effects and draft variations and estimate the form factor with a combined EFD & CFD method. This method is called the two form factor method (Korkmaz et al., 2021b, 2022). The main idea behind it is that combining CFD and EFD at their strong points can result in a more accurate estimation of the form factor and consequently in power prediction. Additionally, a potential alternative or complementary method to the Prohaska approach is to use double-body Reynolds-Averaged Navier–Stokes (RANS) computations, which are also used in the present study. Recently, Quintuña et al. (2024) have implemented a similar approach for form factor estimation combining EFD and CFD methods in order to improve the full-scale resistance prediction.

The two-form factor method estimates the form factor at both the model and the full scale to prevent underestimation of viscous resistance in full scale scenarios, particularly when dealing with wetted transom flow (Korkmaz et al., 2022). This approach involves decomposing the viscous resistance coefficient, C_{PV}, into two components: one proportional to the frictional resistance based on a standard friction line, and another capturing the influence of the flow in the transom region. As noted by Korkmaz et al. (2022), the flow characteristics aft of a submerged transom significantly affect the form factor, justifying this decomposition. Furthermore, Korkmaz et al. (2021a) underscores the value of conducting full-scale CFD simulations, particularly to overcome the limitations of the Prohaska method. These include its assumption of linearity in the correlation of experimental data, which becomes invalid for certain hull forms—such as those with pronounced bulbous bows—thereby introducing greater uncertainty in the form factor estimation.

In addition to the studies mentioned above in the literature, Terziev et al. (2021) indicates that the form factor shows intense variations to low speeds, while it displays negligible variations in higher speeds. Consequently, the form factor is considered Froude number dependent. Korkmaz et al. (2021a) claims that the combination of the EFD and CFD method, together with double-body RANS computations, improves form factor predictions. This study has confirmed that combining EFD and CFD provides a more accurate estimation of form factor and, consequently, of propulsive power within the range of the cases studied, as well as offers improvements to the ITTC-78 method. Minchang et al. (2025) investigate the ITTC-recommended wave pattern resistance analysis by comparing experimental, panel method, and CFD-based predictions for a container carrier model. In their analysis, they have calculated the form factor using the Prohaska method by regression analysis of Fr^4 and the total resistance coefficient in the low Fr range ($\text{Fr} \leqslant 0.227$). They run free-surface CFD simulations for form factor estimation.

Dogrul et al. (2020) conducts a numerical investigation into the scale effects on ship resistance components and the form factor using URANS-based CFD simulations. The study focuses on the hydrodynamic performance of the KCS and KVLCC2 hulls on multiple scales, in order to quantify the influence of scaling on individual resistance components. To this end, the total resistance is decomposed into isolating and examining the contributions of each component. The CFD results are compared with full-scale resistance predictions obtained using different extrapolation methods, highlighting the discrepancies among various predictive techniques. The study further explores the hydrodynamic behavior at different scales, improving our understanding of scale-dependent phenomena in ship resistance. Key findings include a near-constant residual resistance coefficient for KCS across scales, while KVLCC2 exhibits a decreasing trend in residual resistance with increasing Reynolds number. Additionally, the simulations reveal thinner boundary layers and narrower stern wakes for larger-scale models, along with distinct variations in wave patterns between the two hull forms.

Kuiquan et al. (2024) introduced the concept of Hull Fouling Factors (HFFs) to quantify the time-varying influence of hull roughness on main engine load (MEL) using AIS, operational, and environmental data. Employing a Random Forest model, the authors demonstrated that roughness effects increase with days since cleaning, particularly for vessels operating on sea routes, highlighting the importance of route-dependent fouling behavior for resistance and energy performance analysis. Ji-Woo et al. (2024) present an experimental study in the CNU Cavitation Tunnel investigated how different surface roughness heights on flat plates affect boundary layer development and drag across a range of Reynolds numbers. The findings showed that increasing roughness enhances boundary layer thickness and frictional resistance, offering valuable insights into the hydrodynamic mechanisms by which hull roughness influences form factor estimation and overall ship resistance.

Lopes et al. (2025) investigate the prediction of ship resistance using RANS-based CFD at both model and full scale, comparing their simulations with historic experimental measurements. Their study revealed systematic under-prediction of full-scale resistance, which they attributed primarily to the neglect of surface roughness and the assumption of an even-keel condition, highlighting the persistent challenge of scale effects in CFD-based resistance prediction. They also applied the ITTC 1978 scaling procedure to model-scale CFD results, demonstrating that scaled predictions could overestimate resistance when roughness and air resistance are accounted for. These findings underscore the importance of accurate scale modeling and validate the need for methods that can reconcile model- and full-scale discrepancies. In this context, the 2−k method offers a complementary approach by improving the estimation of the form factor across scales, particularly for hulls with wetted transoms, and by systematically addressing the sensitivity to grid resolution and draft variations observed in CFD predictions.

In this study, a systematic analysis of scale effects, as well as variations in roughness and draft, is carried out by comparing the numerically calculated form factors with available experimental data. The combined EFD&CFD form-factor calculation approach and its improvement (the 2−k form factor) proposed by Korkmaz et al. (2021b, 2022) was applied to calculate the form factor and assess possible improvement in the extrapolation procedure from model to full-scale (1978 ITTC Performance Prediction Method ITTC, 1978) The main research question can be summarized as follows:

How are the form factors obtained from CFD simulations using the 2–k approach influenced by scale effects, hull roughness, and variations in draft?

Five benchmark hulls have been used, including the JBC, KCS and ONRT from the Tokyo (2015) workshop, KVLCC2 and DTMB 5415 from the Simman (2008) workshop, as well as two commercial hulls from the FORCE Technology database. This study also constitutes an extended investigation to Korkmaz et al. (2021b, 2022), applying additional benchmarks and commercial hulls to contribute to the effectiveness of the combined EFD&CFD form factor method.

The outline of this article is organized as follows. Section 2 introduces the theoretical background, form factor concept by EFD procedures and the *2–k* method. In Section 3, the setup of the CFD simulations is described. In Section 4, the test cases used in this study are presented. The results of the Verification and Validation (V&V) analysis are demonstrated in Section 5. The results of the study and the discussions are presented in Section 6, while the final observations are summarized in Section 7.

2. Theoretical background

A brief description of the governing equations, which describe the CFD simulations, is presented. Additionally, in this section, the experimental determination of the form factor and the *2–k* method are shown.

2.1. Governing equations

The fundamental equations governing fluid flow are the continuity and Navier–Stokes equations, which form a system of nonlinear partial differential equations derived from the conservation laws of mass and momentum. To express these equations more concisely, Cartesian tensor notation is employed—where vector components are denoted using a single index and tensor components with two indices. Additionally, Einstein's summation convention further simplifies the notation by implying summation over repeated indices. Accordingly, the continuity equation (Eq. (1)) and the Navier–Stokes equation (Eq. (2)) for an incompressible, Newtonian fluid are given as follows:

$$\frac{\partial u_i}{\partial x_i} = 0 \tag{1}$$

$$\frac{\partial u_i}{\partial t} + u_j \frac{\partial u_i}{\partial x_j} = -\frac{1}{\rho}\frac{\partial p}{\partial x_i} + F_i + v\frac{\partial^2 u_i}{\partial x_j \partial x_j} \tag{2}$$

where i and j are the abscissa and ordinate, respectively, u_i represents the velocity components, x_i are the three coordinate components, F_i are the external forces, and v is the kinematic viscosity.

2.2. Experimental and empirical determination of form factor

The determination of the form factor is usually based on three different approaches (Watanabe, 1973). To derive a first estimate of the form factor, Watanabe (1973) introduced the following empirical expression (Eq. (3)).

$$k = -0.095 + 25.6 \cdot \frac{C_B}{(L/B)^2\sqrt{B/T}}. \tag{3}$$

Eq. (3) is only used in conjunction with the ITTC (1957) formula, see Eq. (4).

$$C_F = \frac{0.075}{(log\,Re - 2)^2} \tag{4}$$

The second widespread way to define form factor is by running the model at low speed, where wave making resistance becomes negligible, and thus the friction is the only contributor in total resistance Hughes (1954). In this approach, the frictional resistance coefficient C_F is calculated using the ITTC57 formula (Eq. (4)). The form factor can also be calculated using the formula Eq. (5), where C_F was derived from CFD simulations (CFD-based form factor).

$$(1+k) = \frac{C_F + C_{PV}}{C_F} = \frac{C_V}{C_F} \tag{5}$$

Prohaska method is the third approach to define the form factor and is considered the most common and reliable (Watanabe, 1973). This method is applied in the present study for the systematic analysis of transom submergence. The main idea of the Prohaska method is the expression of the wave-making resistance coefficient C_W with the representation of the asymptotic expansion. After neglecting the components of the highest order from the asymptotic expansion, the linear expression of Eq. (6) arises:

$$C_{TM}/C_F = (1+k) + a \times Fr^4/C_F. \tag{6}$$

Notable advancements have been made in model-to-ship correlation through the adoption of the Prohaska method. As reported by Prohaska (1966), an analysis of results from 200 model tests revealed that, for the majority of models, the ratio C_T/C_F tends to align linearly within the Froude number range of $0.1 < Fr < 0.2$. This observation supports the effectiveness of the method in simplifying the extrapolation of model-scale results to full scale.

Despite their widespread use, both Hughes' and Prohaska's methods present notable limitations. In the case of Hughes' approach, testing hull models at low speeds may induce laminar flow conditions, potentially leading to an underestimation of the frictional resistance. The Prohaska method also exhibits fundamental drawbacks, particularly when applied to hulls featuring bulbous bows, twin-screw configurations with appendages, or full stern forms. In such cases, the observed C_T/C_F values deviate from the expected linear trend, thereby reducing the method's reliability. Consequently, there is a pressing need to explore alternative strategies—particularly those based on CFD—to enhance the accuracy of form factor estimation. This becomes especially relevant for modern hull forms, such as those with partially submerged bulbous bows under intermediate loading conditions or with deeply submerged transom sterns.

2.3. The two form factor (2–k) method

As mentioned in the previous paragraph, the form factor can be assessed using different methods (such as Hughes and Prohaska) but all of them have limitations or shortcomings. . For instance, the main problem with the Hughes method (Hughes, 1954) is the difficulty of stimulating turbulent flow around the hull since the resistance test must be carried out at very low Re and Fr numbers for estimating the form factor. Also, the measurements can be considered vulnerable due to the uncertainties involved in measuring minor forces. For these reasons, Prohaska (1966) recommended a simplified process for extracting the form factor from resistance testing, with specific assumptions. If these assumptions are not satisfied, the Prohaska approach may fail.

The recirculation region behind the transom, which is one of the challenges of the Prohaska method, is assumed to be the same for all Re numbers from model to full-scale. This leads to an under-prediction of viscous resistance at full-scale. To address this problem, the model-scale decomposition of the viscous resistance coefficient (C_{PVM}), also known as form resistance, is introduced as shown in Eq. (7) (Korkmaz et al., 2022)

$$C_{PVM} = C'_{PVM} + C_{trM}, \tag{7}$$

where C'_{PVM} represents the proportional part to C_F based on the criteria of Hughes (1954), and C_{trM} corresponds to the resistance due to the flow separation behind the transom which is not proportional to C_F. According to Korkmaz et al. (2022), C_{trM} does not change substantially from model to full-scale Re number, while C'_{PVM} remains scale proportional to C_F. Since such different scaling trends of C_{trM} and C'_{PVM} cannot be sustained by a single Re independent form factor, CFD form factor predictions in model and full scale must be used for its correction or prompt estimation for hulls with a wetted transom.

The aforementioned methodology is called the two form factor (2–k) method and certain steps are needed for its application. Firstly, towing tank testing provides the model-scale total resistance coefficient C_{TM}. Afterwards, either the Prohaska method (Prohaska, 1966) or CFD simulation (Korkmaz et al., 2021a), is used to calculate the form factor in model-scale k_M. Then, the wave resistance coefficient C_W is estimated by using Eq. (8).

The methodology described above is known as the two-form factor (2–k) method, and its implementation involves a series of defined steps. Initially, towing tank experiments are conducted to obtain the model-scale total resistance coefficient, C_{TM}. Subsequently, the model-scale form factor, k_M, is determined using either the Prohaska method (Prohaska, 1966) or computational fluid dynamics (CFD) analysis (Korkmaz et al., 2021a). Once k_M is known, the wave resistance coefficient, C_W, can be calculated using Eq. (8).

$$C_W = C_{TM} - \left(1 + k_M\right) C_{FM} \tag{8}$$

C_W is derived by using the model-scale form factor, while viscous resistance coefficient C_V is extracted by using the full-scale form factor (Korkmaz et al., 2022).

In Fig. 1, the aforementioned process of the 2–k method is presented in the form of a flowchart for better clarity. The case of a submerged transom is also included in the workflow, as studied by Korkmaz et al. (2022). The contribution from the transom form factor is implicitly included in the full scale form factor and can be called as "transom correction". Through the transom form factor correction (k_{tr}), the full scale form factor (k_S) is aimed to be achieved. It is given by Eq. (9) where if $tr_{ra} \leqslant 0.025$ then $k_{tr} = 0$ and if $tr_{ra} > 0.025$ the $k_{tr}0$ is calculated by Eq. (10):

$$k_S = k_M + k_{tr} \tag{9}$$

An empirical correction formula, Eq. (10), has been proposed by Korkmaz et al. (2022) through regression analysis. This formula is established to include the effect of recirculation in the wake of transom due to its submergence.

$$\begin{aligned} k_{tr} = {} & [-0.025 + tr_{ra}(1.5 - 2.3tr_{ra} - 0.07LCB)] \times [-5.45 + \log_{10}(\overline{Re_M}) \\ & \times (1.415 + 4.32tr_{ra}) - (\log_{10}(\overline{Re_M}))^2(0.081 + 0.55tr_{ra})] \end{aligned} \tag{10}$$

In Eq. (10), $\overline{Re_M}$ is the average Reynolds number on the model-scale and LCB is relative to $L_{PP}/2$. By comparing the k_{tr} values from CFD and the empirical correction formula Eq. (10), the two methods demonstrate minor discrepancies, as shown in Section 6. Eq. (11) expresses the percentage of transom submergence and is used to apply the empirical formula.

$$tr_{ra} = \frac{A_{tr}}{A_{max}} \tag{11}$$

where A_{tr} is the area of the submerged transom, A_{max} is the maximum cross-section area for a given draft and y_{tr} is the transverse dimension of the wetted transom. Based on Korkmaz et al. (2022), the lower limit for tr_{ra} is established ($tr_{ra} \leqslant 0.025$), as lower values can result in a partially wetted or dry transom flow.

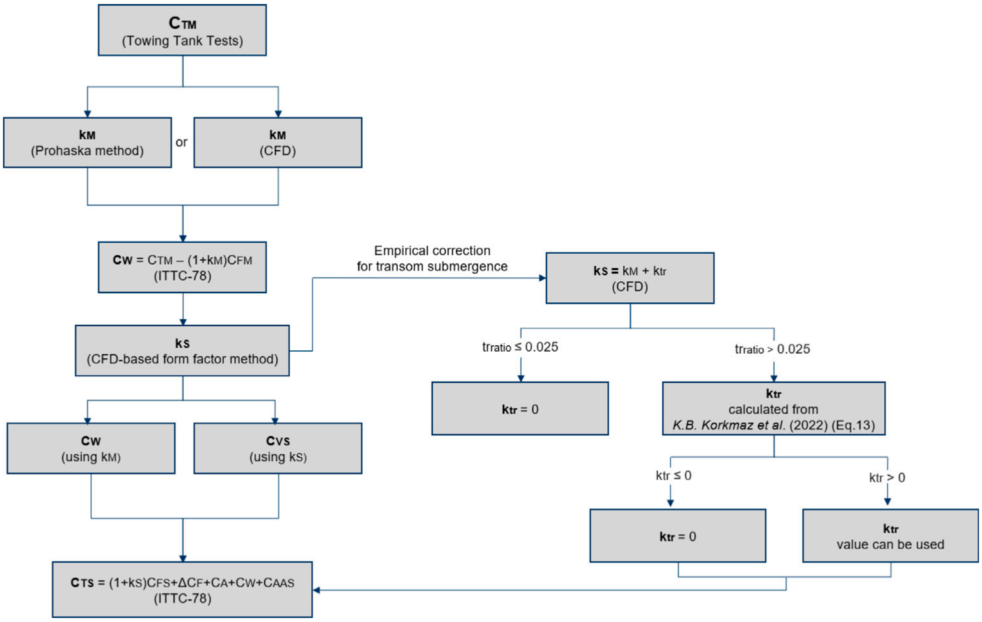

Fig. 1. Flow chart of total resistance calculation in full scale based on ITTC-78 guidelines applying the *2–k* method in case of transom submergence.

3. CFD simulations setup

The computational domain and boundary conditions of the CFD simulations setup are presented, along with an illustration and commentary on the generated mesh. Additionally, the computational approaches (Double Body and Free-Surface) being used are detailed. A description of the roughness modeling is also presented.

3.1. Computational domain, boundary conditions and mesh generation

A body-fixed reference frame $x_0y_0z_0$ is established at the ship's initial center of gravity (COG) position, moving in accordance with the hull's motions and instantaneous velocity. The dimensions of the computational domain and the associated refinement zones are defined relative to this body-fixed coordinate system. Fig. 2 presents the side and front views of the computational domain for both modeling approaches. The domain itself is a rectangular prism designed to replicate a towing tank environment, with its size adjusted based on the hull's scale factor in each simulation. Detailed illustrations of the computational domain, the nomenclature for its seven boundaries, and their dimensions for the double-body (DB) and free-surface (F-S) methods are shown in Figs. 2(a) and 2(b), respectively.

A symmetry plane is applied due to the flow's bilateral symmetry (starboard and portside), effectively handling the computational cost. Furthermore, grid refinement zones are strategically employed to resolve sharp gradients in flow variables such as velocity and pressure. Refinement near the hull geometry is consistently applied along all three spatial dimensions—longitudinal, transverse, and vertical. Since the double-body assumption neglects free surface effects, no additional refinement zones are necessary in that approach. The computational grids for all test cases, across both DB and F-S methods and at both model and full scales, consist of orthogonal hexahedral cells. The total cell counts for each approach and scale are summarized in Table 1. Specifically, the DB model incorporates one refinement zone adjacent to the hull, whereas the F-S model includes four additional refinement zones located at the free surface, bow, stern, and transom wake regions.

To accurately resolve both frictional and turbulent effects, prism layering is employed as a meshing technique to capture the boundary layer near the hull surface. The properties of this prism layering—such as the number of layers and their thickness—are adapted based on the simulation scale (model or full-scale) and the scale factors applied in the sensitivity analysis. In this study, ten prism layers are used for both model types, with layer thicknesses progressively increasing away from the wall towards the far field.

Table 1
Number of cells in double body and free surface approach in both model and full-scale for all studied hulls.

Test case	Double body method		Free surface method	
	Model-scale [×10^7]	Full-scale [×10^7]	Model-scale [×10^7]	Full-scale [×10^7]
JBC	0.565	1.002	0.982	1.318
KCS	0.544	0.997	0.912	1.265
KVLCC2	0.685	1.142	1.122	1.439
DTMB 5415	0.493	0.875	0.810	1.112
ONRT	0.501	0.924	0.852	1.135
180K DWT BC	0.631	1.081	1.008	1.376
82K DWT BC	0.512	0.896	0.873	1.140

Both the prism layer thickness and the wall-normal distance are dependent on the Reynolds number (*Re*), since the flow regime—laminar or turbulent—is significantly influenced by flow velocity. The number of prism layers and the stretching factor, λ_s, which defines the ratio of the thickness of each successive layer to the previous one, together control the total thickness of the boundary layer mesh and its capacity to capture turbulence within the near-wall region. The mesh setup for the double-body (DB) and free-surface (F-S) approaches, including refinement zones at the fore and aft sections of the hull and the prism layering configuration, is illustrated in Fig. 3.

Fig. 4 shows the y^+ distribution in both model and full-scale. The values of y^+ in model scale have been kept in viscous sublayer and buffer region, while the y^+ takes values along the entire boundary layer in full scale. One can observe that there is a discrepancy between the model and full-scale in the aft and fore parts of the three test cases, because the geometry changes abruptly in these regions, leading to a rapid change of tangential flow velocity. Specifically, the displacement effect; accelerated flow at the bow region, especially, around low pressure regions and the boundary layer development in the stern are the main contributors to this abrupt change of flow speed. Moreover, the Reynolds numbers for these test cases are different, which also results

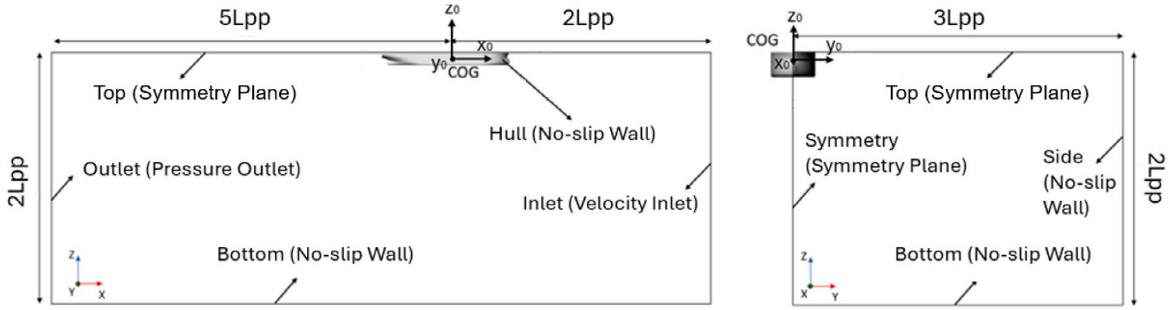

(a) DB approach

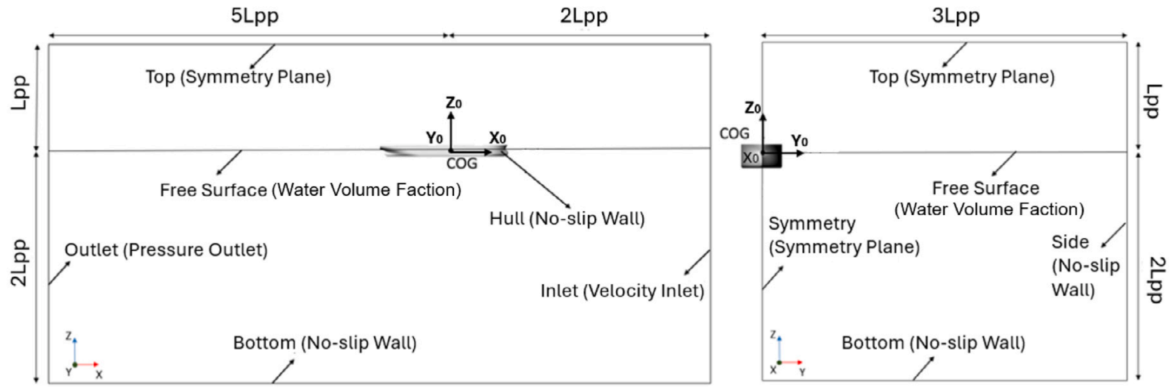

(b) F-S approach

Fig. 2. Representation of the computational domain dimensions and applied boundary conditions for (a) Double-Body (DB) and (b) Free-Surface (F-S) approaches at both model- and full-scale. Left: Starboard side view; Right: Front view.

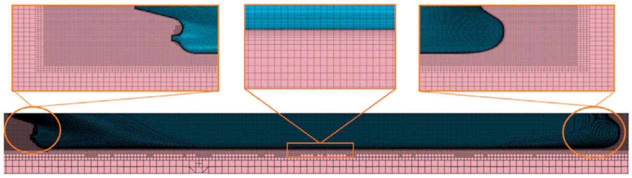

(a) DB model

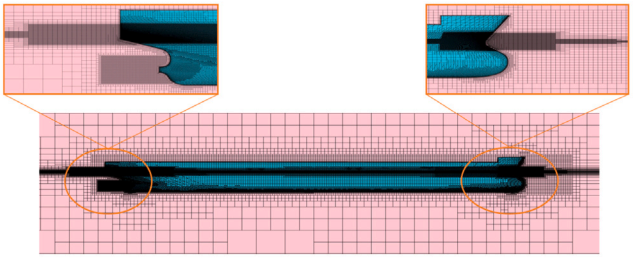

(b) F-S model

Fig. 3. Close-up views of the generated mesh around the bow and stern regions for both double-body (DB) and free-surface (F-S) numerical simulations (side view — JBC).

in different boundary layer profiles and thus shear stress distribution in the aft part of these models.

The study is carried out in fresh water at 15°C with a density of $\rho = 999.1\ \mathrm{kg/m^3}$ and a kinematic viscosity of $\nu = 1.1386 \times 10^{-6}\ \mathrm{m^2/s}$ at a speed of (Froude number or $Fr = U/\sqrt{gL} = 0.1$).

3.2. Numerical models

In the following sections, the details of the two main simulation strategies are presented, specifically the Double-Body and the free-surface approaches, showing their assumptions, limitations, and advantages.

3.2.1. Free-surface model including dynamic fluid body interaction

For a more accurate prediction of the flow around a hull, free surface computation is crucial, especially at higher Froude numbers, since the generated waves have a significant contribution to the total ship resistance. Besides the importance of capturing hull-generated waves, in the context of this work, free surface simulations were carried out to capture the flow behind the submerged transom to study the impact of the wetted transom on the form factor. The Volume of Fluid (VoF) technique is employed in order to model the fluid interface of a free surface, using the approach of High-Resolution Interface Capturing (HRIC). The two fluid phases, namely water and air, are determined by their respective phase volume fraction (α). α is defined as a numerical value between zero and one, and is determined by the following calculation:

$$\frac{\partial \alpha}{\partial t} + \nabla \cdot (\alpha u) = 0 \tag{12}$$

Fluid density and viscosity are calculated as:

$$\rho = \alpha \cdot \rho_w + (1 - \alpha) \cdot \rho_\alpha \tag{13}$$

$$\mu = \alpha \cdot \mu_w + (1 - \alpha) \cdot \mu_\alpha \tag{14}$$

where subscripts α and w indicate air and water, respectively. The fluid-ship interaction is considered a decisive factor for the assessment of resistance. Through considering the aforementioned interaction in the simulations, sinkage and trim of the hull are obtained. Since the hull

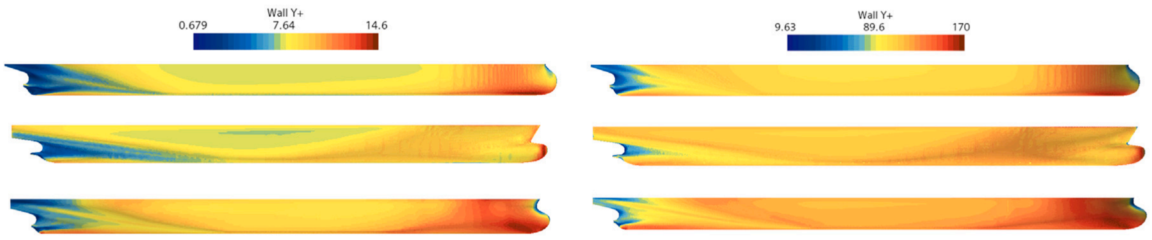

(a) Model-scale

(b) Full-scale

Fig. 4. Wall y^+ visualization on the hull of JBC (top), KCS (middle) and KVLCC2 (bottom) at $Fr = 0.1$ (side view).

sinkage and trim are of interest in this study, only two fundamental Degrees of Freedom (DoF) of the hull are taken into account in still water. To this end, the Dynamic Fluid-Body Interaction (DFBI) method is employed (STAR-CCM+, 2023). Finally, an implicit-unsteady solver is used in conjunction with the VOF-HRIC and the FBI approaches.

3.2.2. Double-body approach

The *Double-Body* (DB) approach is a simulation technique grounded on the assumption that free-surface effects are negligible at very low speeds, where wave-making resistance contributes minimally to the overall resistance. This assumption is implemented by applying a symmetry boundary condition at the plane corresponding to the undisturbed free surface, effectively eliminating free-surface interactions in the CFD analysis. According to Yao et al. (2021), the DB approach is both appropriate and efficient for Froude numbers below 0.142, where wave generation by the hull is insignificant. Furthermore, DB simulations offer a substantial reduction in computational cost compared to free-surface methods, as they omit free-surface modeling and typically employ steady-state solvers.

3.2.3. Roughness modeling

The traditional approach in experimental testing to account for hull roughness effects involves adding a frictional resistance correction term derived from empirical formulas. This concept of a roughness allowance was initially proposed by Townsin and Mosaad (1985) and later adopted by 19th Committe ITTC (1990).

$$\Delta C_F = 0.044\left[\left(\frac{AHR}{L_{WL}}\right)^{\frac{1}{3}} - 10Re^{-\frac{1}{3}}\right] + 0.000125 \tag{15}$$

Here, AHR denotes the average hull roughness, and L_{WL} represents the waterline length. To incorporate roughness effects in numerical simulations, specialized models have been developed that account for wall roughness impacts on the local flow near the hull surface. The fundamental principle of roughness modeling is to shift the logarithmic layer of the turbulent boundary layer closer to the wall, which is typically implemented by modifying the wall functions. For instance, in STAR-CCM+ (2023), the default wall treatment employs the roughness function f formulated by Cebeci and Bradsaw (1977), albeit applied in a generalized manner as follows:

$$f = \begin{cases} 1 & \text{if } R^+ \leqslant R^+_{smooth} \\ \left[B\left(\frac{R^+ - R_{smooth}}{R^+_{rough} - R_{smooth}}\right) + CR^+\right]^{\alpha} & \text{if } R^+_{smooth} < R^+ \leqslant R^+_{rough} \\ B + CR^+ & \text{if } R^+ > R^+_{rough} \end{cases} \tag{16}$$

where $B = 0$ and $C = 0.253$ are model coefficients and the exponent, α, is defined as

$$\alpha = sin\left[\frac{\pi}{2}\frac{log(R^+/R_{smooth})}{log(R^+/R_{smooth})}\right] \tag{17}$$

In Eq. (17), R^+ is the roughness Reynolds number, which is defined as:

$$R^+ = \frac{R_S U_\tau}{\nu} \tag{18}$$

where R_S is the equivalent sand-grain roughness height, $U_\tau = \sqrt{\tau_w/\rho}$ is the friction velocity, τ_w is the shear stress at the wall and ν the kinematic viscosity. The roughness function is imported in Eq. (19) to adjust the velocity near the wall,

$$U^+ = \frac{1}{\kappa}ln(Ey^+) - \frac{1}{\kappa}ln(f) \tag{19}$$

where E is the log-law intercept.

In this study, wall roughness is modeled by applying average height roughness on all studied hulls, with values ranging from 150 μm to 250 μm, in increments of 50 μm. The CFD simulations of the roughness analysis have been set up using the equivalent sand grain roughness which is the 30 μm, but the results in this paper are presented in AHR values.

4. Test cases

Five benchmark hulls, i.e. JBC, KCS, KVLCC2, DTMB 5415 and ONRT, are used for the execution of the systematic analysis of the form factor. The 3D CAD models of the investigated benchmark hulls are publicly available through *Tokyo 2015 Workshop on CFD in Ship Hydrodynamics* (Tokyo, 2015) and *Gothenburg 2010 Workshop on Numerical Ship Hydrodynamics* (Larsson et al., 2010). To have a more holistic study and obtain insight into the present investigation, two additional bulk carriers hulls, 180K DWT BC (FORCE, 2021a) and 82K DWT BC (FORCE, 2021b), have been included in the analysis, which is provided from the FORCE Technology database. The main particulars of these hulls in full-scale, as well as the scale factors, are presented in Table 2. The experimental data was obtained from Hino et al. (2015) (JBC), Larsson et al. (2010) (KCS, KVLCC2 and DTMB 5415), as well as FORCE (2021a) (180K DWT BC and 82K DWT BC). Since Mandru and Pacuraru (2021) lacks details on the form factor and friction resistance estimation, comparisons between CFD and EFD results for ONRT were excluded.

5. Verification and validation (V&V) study

Verification and validation (V&V) constitute essential processes for evaluating the accuracy of numerical modeling. Verification involves quantifying the numerical uncertainty inherent in simulations, while validation assesses the modeling uncertainty by comparing simulation outcomes with experimental or analytical reference data to quantify discrepancies. The verification process typically includes iterative and parameter convergence studies, often employing the Generalized Richardson Extrapolation within a multiple solutions framework. Several practical methods have been developed to estimate numerical uncertainty, including the Grid Convergence Index (GCI), the Convergence Factor, and the Factor of Safety.

The simulation's numerical uncertainty (U_{SN}) consists mainly of four uncertainties, as shown in Eq. (20) (Wilson et al., 2001; Stern et al., 2021)

$$U_{SN} = \sqrt{U_G^2 + U_I^2 + U_T^2 + U_P^2} \tag{20}$$

Table 2
Main particulars of the test cases.

Denotation	Symbol	Unit	Value						
			JBC	KCS	KVLCC2	DTMB 5415	ONRT	180K DWT BC	82K DWT BC
Length between perpendiculars	L_{PP}	m	280.00	230.00	320.00	142.00	154.00	283.50	223.00
Length of waterline	L_{WL}	m	285.00	232.50	325.50	142.18	154.00	288.00	227.02
Depth	D	m	45.00	19.00	30.00	–	14.50	24.00	20.10
Maximum beam of waterline	B_{WL}	m	25.00	32.20	58.00	19.06	18.78	45.00	32.25
Draft (Scantling)	T_S	m	16.50	10.80	20.80	6.15	5.49	17.00	12.20
Block coefficient	C_B	–	0.858	0.651	0.810	0.507	0.535	0.920	0.870

where U_G is the grid uncertainty, U_I is the iterative uncertainty, U_T is the time-step uncertainty, and U_P is the uncertainty related to other parameters. For typical simulations in the marine hydrodynamics field (e.g. resistance and self-propulsion simulations), the computational grid may be considered the primary source of uncertainty.

As discussed previously, validation of a numerical simulation is performed by comparing computed results with corresponding experimental measurements. This process evaluates the modeling uncertainty (U_{SM}) by analyzing experimental data alongside estimating both the sign and magnitude of the modeling error δ_{SM}. Two key parameters are involved in the validation procedure: the validation comparison error (see Eq. (21)) and the validation uncertainty (see Eq. (22)) (ITTC, 2008).

$$E = D - S = \delta_D - \left(\delta_{SM} + \delta_{SN}\right) \tag{21}$$

$$U_V^2 = U_{SN}^2 + U_D^2 \tag{22}$$

where E is the comparison error, S is the solution of simulation, D is the solution from experiment, δ_D is the difference between experimental and real data, δ_{SN} is the simulation error, U_D is the uncertainty of the data from the experiments, and U_V validation uncertainty. Here, E denotes the comparison error, S is the simulation result, and D represents the experimental measurement. The term δ_D corresponds to the discrepancy between the experimental data and the true value, while U_D indicates the simulation error. Additionally, U_D refers to the uncertainty associated with the experimental data, and U_V represents the overall validation uncertainty.

Finally, once the validation comparison error and validation uncertainty have been determined, the validation outcome can be classified into two distinct categories:

- When $|E| > U_V$, the errors in both the experimental data D and simulation results S exceed the validation uncertainty U_V, indicating that validation has not been achieved at this level of uncertainty. The magnitude of U_V reflects the degree of confidence in the CFD model's predictive capability.
- For $|E| < U_V$, all errors in both D and S are smaller than U_V and thus validation is achieved in the U_V interval (ITTC, 2008). When $|E| \ll U_{val}$, the δ_{SM} indicates that the numerical models implemented in the simulation need to be improved.

For the test cases examined in this study, the experimental uncertainty of the KCS towing tank measurements in calm water was obtained from the FORCE Technology database (Otzen, 2010). Due to the absence of uncertainty data for U_V for the JBC and the two commercial hulls, the value from the KCS test, $U_D = 0.95\%$, is adopted as a validated reference for their validation assessment. The experimental uncertainties for the other benchmark hulls, KVLCC2 and DTMB 5415, are sourced from the *Gothenburg Workshop, 2010* dataset. Verification and validation (V&V) results (MARIN, 2022; Larsson and Raven, 2010; Eca and Hoekstra, 2014) are summarized in Table 3. The principal parameter of interest is $C_T = (1+k)C_F + C_W$, with numerical results corresponding to simulations that include free-surface effects (F-S setup). As shown in Table 3, all simulations satisfy the validation criterion $|E| < U_V$, indicating that the numerical results are consistent with experimental uncertainty and thus considered validated.

Grid refinement studies were performed in accordance with the GCI methodology outlined by Tezdogan et al. (2015). Each convergence assessment was based on three sequential simulations employing systematically refined spatial discretization. In the grid-spacing study, three meshes were generated by uniformly coarsening the baseline grid in all directions, while maintaining all other simulation parameters, including the time step unchanged. The mesh-convergence evaluation was therefore carried out using a constant time step.

To evaluate whether the solution exhibited convergence, the convergence ratio r was calculated as:

$$r = \frac{e_{k21}}{e_{k32}} \tag{23}$$

where $e_{k21} = u_{k2} - u_{k1}$ and $e_{k32} = u_{k3} - u_{k2}$ represent the differences between the medium and fine solutions and between the coarse and medium solutions, respectively. Here, the u_{k1}, u_{k2} and u_{k3} and denote the results obtained using the fine, medium, and coarse values of the input parameter k, that is the grid spacing.

For convergence conditions, the generalized Richardson Extrapolation (RE) method is applied to predict the error and order of accuracy (p_k) for the selected k_{th} input parameter. For a constant refinement ratio r_k, p_k can be calculated by:

$$p_k = \frac{ln(e_{k32}/e_{k21})}{ln(r_k)} \tag{24}$$

The extrapolated values can be estimated as (Tezdogan et al., 2015):

$$\phi_{ext}^{21} = (r_k^p\phi_1 - \phi_2)/(r_k^p - 1) \tag{25}$$

The approximate relative error and extrapolated relative error can be estimated via Eqs. (26) and (27) (Tezdogan et al., 2015):

$$e_a^{21} = \left|\frac{\phi_1 - \phi_2}{\phi_1}\right| \tag{26}$$

$$e_{ext}^{21} = \left|\frac{\phi_{ext}^{12} - \phi_1}{\phi_{ext}^{12}}\right| \tag{27}$$

The fine grid convergence index is calculated by:

$$GCI_{fine}^{21} = \frac{1.25e_a^{21}}{r_k^p - 1} \tag{28}$$

In this study, a constant refinement ratio of $\sqrt{2}$ was applied for the mesh-spacing and convergence analyses. It is important to note that, during the mesh convergence study, the surface mesh on the ship hull was kept unchanged to ensure an accurate representation of the vessel. The final number of mesh cells for each configuration, based on the applied refinement ratio, is presented in Table 4. Table 5 presents the verification parameters of the three resistance coefficients for the grid-spacing study in full scale. As can be seen from Table 5 the estimated uncertainties for the obtained parameters were relatively low. The numerical uncertainties in the finest-grid solution for C_F, C_{VP} and C_V are predicted as 0.02, 0.01 and 0.08 % for DB model and 0.01, 0.04 and 0.09 for F-S model.

In addition to the V&V analysis conducted using free-surface (F-S) simulations at model scale for all benchmark hulls, a dedicated investigation has been performed to assess discretization uncertainties—specifically grid and iterative errors—for the double-body (DB) simulation approach. This study focuses on a single benchmark case, the JBC

Table 3
Results from V&V analysis of model-scale total resistance coefficient C_T at Fr = 0.1 for the finest grid using k-ω SST turbulence model.

Test case	$C_T \times 10^{-3}$ [–] (CFD)	$C_T \times 10^{-3}$ [–] (EFD)	p[–]	E [%]	U_D [%]	U_{SN} [%]	U_V [%]	Comparison
JBC	4.34	4.29 (Hino et al., 2015)	0.58	−1.15	0.95	3.05	3.19	$\|E\| < U_V$
KCS	3.62	3.80 (Larsson et al., 2010)	1.16	4.70	0.95	5.17	5.26	$\|E\| < U_V$
KVLCC2	4.23	4.11 (Larsson et al., 2010)	0.75	−2.84	0.42	4.23	4.28	$\|E\| < U_V$
DTMB 5415	2.91	2.85 (Larsson et al., 2010)	0.34	0.13	0.51	7.93	7.95	$\|E\| < U_V$
ONRT-appended	4.25	4.32 (Mandru and Pacuraru, 2021)	1.68	1.6	0.44	9.25	9.26	$\|E\| < U_V$
180K DWT BC	4.64	4.48 (FORCE, 2021a)	1.04	−3.44	0.95	4.94	5.03	$\|E\| < U_V$
82K DWT BC	4.03	4.15 (FORCE, 2021b)	0.87	2.89	0.95	5.22	5.30	$\|E\| < U_V$

Table 4
The resulting number of cells for each mesh configuration obtained from the mesh convergence study in full scale for both modeling approaches.

Mesh configuration	Total cell number (DB)	Total cell number (F-S)
Fine	10,020,000	13,180,000
Medium	6,325,000	9,585,000
Coarse	3,170,000	5,990,000

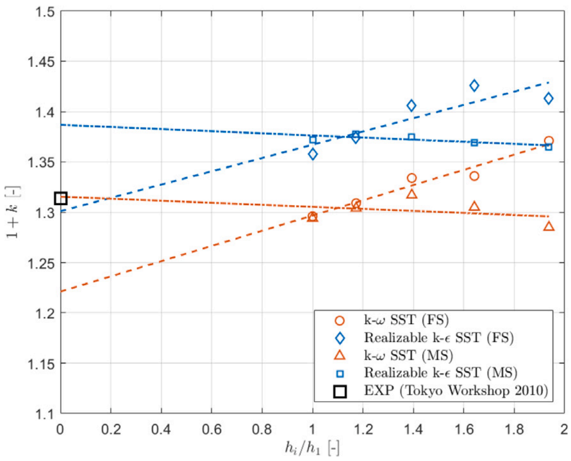

Fig. 5. Sensitivity analysis of the form factor for the JBC test case through grid refinement, comparing k − ω SST and realizable k − ϵ turbulence models at both model scale (MS) and full scale (FS).

hull, and considers both model- and full-scale computations using two different turbulence models. The objective is to evaluate the influence of grid refinement on the CFD-based form factor prediction, with the results summarized in Fig. 5. The analysis presents the variation of the computed $1+k$ values as the mesh is progressively refined, maintaining a constant refinement ratio throughout.

This investigation also serves to assess the suitability of the two turbulence models across both scales by comparing CFD results to experimental data from the Tokyo Workshop, 2010. Linear regressions are fitted to the CFD data to estimate the asymptotic value of the form factor as the grid size approaches zero, i.e., $h_i/h_1 \rightarrow 0$. The refinement ratio explored in this study ranges from $1 < h_i/h_1 < 2$. For the full-scale (FS) simulations, $h_i/h_1 = 1$ corresponds to a base grid where the cell size matches the geometric scale factor ($\lambda = 40$), while $h_i/h_1 = 2$ represents a grid with double the base cell size. In the model-scale (MS) case, the domain is scaled down by a factor of 40, making $h_i/h_1 = 1$ indicative of the coarse mesh.

Based on k −ω the results presented in Fig. 5, the k − ω SST turbulence model is identified as the most suitable choice for simulations at both model (MS) and full scale (FS). This preference is attributed to the model's enhanced capability to resolve the boundary layer (BL) flow, offering improved accuracy near the wall. The computed values of $1+k$ result from the combination of the frictional resistance coefficient C_F, determined using the ITTC57 line, and the viscous resistance coefficient C_V, obtained from CFD simulations. Notably, the two turbulence models yield markedly different outcomes, as illustrated by the deviations in CFD predictions compared to experimental data in Fig. 5. When comparing CFD to EFD data, the k − ω SST model shows a discrepancy of –1.5 % in FS and –2.1 % in MS. In contrast, the realizable k − ϵ model aligns closely with full-scale experimental data but overpredicts by 4.3 % in model-scale. Consequently, the k −ω SST model is deemed the most appropriate for the objectives of this study.

Beyond the grid refinement sensitivity study, grid uncertainty has also been assessed for both scales and turbulence models. The results, shown in Figs. 5 and 6, correspond to the JBC test case and aim to provide a comprehensive evaluation of grid-related uncertainties. Since systematic grid refinement is the only variable introduced, this analysis helps isolate its effect on the solution accuracy across all test cases and modeling approaches. The uncertainty estimation follows the methodology proposed by MARIN (2022), based on the framework of Eca and Hoekstra (2014).

The uncertainty analysis results for model-scale simulations, displayed in Fig. 6, indicate consistent behavior across refinement levels, evidenced by the relatively low uncertainty values. This consistency supports the reliability of the grid convergence trend and highlights the influence of each turbulence model on the solution. The uncertainty values reported in the legend of each graph refer to the case with refinement ratio $h_i/h_1 = 1$. Furthermore, Table 6 presents the asymptotic values of resistance components and the form factor, extrapolated from the uncertainty analysis. These asymptotic values represent an estimate of the variable's behavior as the cell count approaches infinity, i.e., $n \rightarrow \infty$.

In Figs. A.1 and A.2 of Appendix the iterative error of C_F is presented in MS and FS, respectively. The selection of C_F for the study of iterative error is made and details are available in Appendix.

Considering the findings from both the model-scale (MS) and full-scale (FS) convergence studies, it can be concluded that, for the selected grid densities and refinement ratios, all results obtained using the k − ω SST turbulence model lie within the asymptotic range. This outcome confirms the model's reliability and suitability for the simulations conducted. Additionally, the convergence behavior of the three resistance components does not exhibit uniform trends. This divergence is expected, as the turbulent kinetic energy and specific dissipation rate—key variables in the turbulence model—are governed by distinct differential equations. As a result, variations in convergence and uncertainty arise, even though the resistance components are inherently interdependent.

6. Results

6.1. Scale effect

An investigation of various scaling factors has been carried out. In particular, the study examines how systematically altering the scale of the JBC, KCS, and KVLCC2 hulls influences the coefficients C_F, C_{PV} and C_V. Beyond the model and full-scale configurations, six additional scale factors ($\lambda_i = \lambda/16, \lambda/8, \lambda/4, \lambda/3, \lambda/2$) have been explored using the F-S model.

Table 5

Grid convergence study for the three resistance coefficients and both DB and F-S models in full scale.

	Double-body			Free-Surface		
	C_F	C_{VP}	C_V	C_F	C_{VP}	C_V
	(with monotonic convergence)			(with monotonic convergence)		
r	$\sqrt{2}$	$\sqrt{2}$	$\sqrt{2}$	$\sqrt{2}$	$\sqrt{2}$	$\sqrt{2}$
ϕ_1	0.07520	0.02390	0.12550	0.07615	0.02441	0.13240
ϕ_2	0.07630	0.02430	0.11730	0.07702	0.02495	0.12370
ϕ_3	0.07860	0.02530	0.10100	0.07910	0.02584	0.10700
R	0.478	0.400	0.503	0.418	0.607	0.521
p	4.97	6.18	4.63	8.21	4.71	6.14
ϕ_{ext}^{21}	0.07419	0.02363	0.13380	0.07578	0.02387	0.13825
e_{α}^{21} (%)	0.01	0.02	0.07	0.01	0.02	0.07
e_{ext}^{21} (%)	0.01	0.01	0.06	0.005	0.02	00.4
GCI_{fine}^{21} (%)	0.02	0.01	0.08	0.01	0.04	0.09

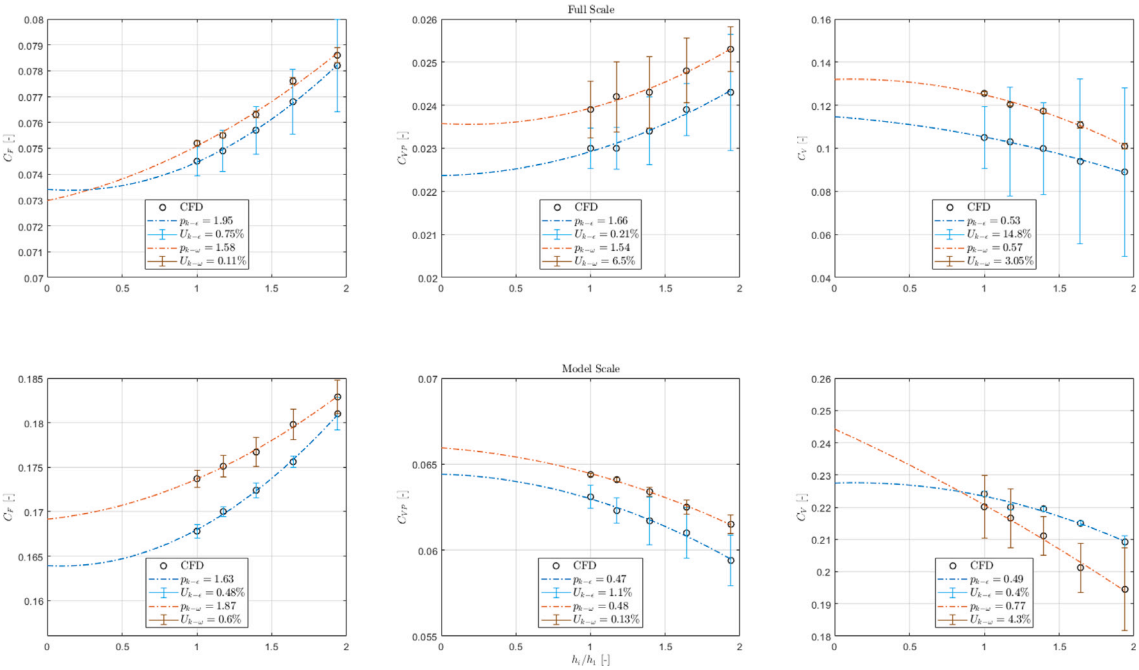

Fig. 6. Convergence of C_F, C_{PV} and C_V with grid refinement ratio for the JBC hull. Data fits correspond to refinement ratios $1 \leqslant h_i/h_1 \leqslant 2$ for k $-$ ω SST and realizable k $-$ ϵ turbulence models at both model scale (MS) and full scale (FS).

Table 6

Asymptotic values of C_F, C_{PV}, C_V and k for JBC.

Scale	Turbulence model	C_F [ITTC57]	C_{PV} [CFD]	C_V [CFD]	1+k [–]
FS	k-ω SST	0.073	0.024	0.132	1.225
	Realizable k-ϵ	0.073	0.022	0.118	1.301
MS	k-ω SST	0.169	0.066	0.244	1.314
	Realizable k-ϵ	0.169	0.064	0.229	1.355

The resistance components computed from the test cases studied in different Reynolds numbers, representing different scale factors, are shown in Fig. 7. In these plots, $Re = 5.225 \times 10^6$ corresponds to the model-scale, while the $Re = 1.322 \times 10^9$ indicates the full-scale case. It is obvious from the depicted results that the extracted values of all three test cases and all the resistance coefficients show a parabolic declining trend from model-scale to full-scale. Moreover, one can observe that C_F is approximately 70 % larger than C_{VP} for all scale factors. This split is expected, as C_F is the main contributor to the total resistance at low Fr. Furthermore, the results indicate that KCS has the lowest resistance components, since it is the only slender hull in this analysis. Among the resistance components of all the studied hulls, C_{VP} has the largest discrepancy. The C_{VP} is typically more influenced by flow in transverse directions and eddy-making pressure distribution around the body, which may vary more significantly between models. Based on the depicted results and the observations above, the transition from model to full-scale influences the resistance coefficient components, which is also visible in the form factor results shown later in this section.

Fig. 8 on top depicts the comparison between the ITTC57 friction line and the CFD results for JBC, KCS, and KVLCC2. From our CFD computations, the frictional resistance coefficient includes additional effects such as curvature and transverse flows, reflecting form resistance rather than pure friction. As a result, CFD-derived C_F values are typically higher compared to theoretical friction lines designed for zero pressure gradient scenarios. The ITTC-57 line, however, is not a pure friction line but an engineering approximation, adjusted for specific purposes, and it shows significantly larger values at model-scale Reynolds numbers. At higher Reynolds numbers (beyond $Re \approx 1 \times 10^8$), the C_F values from CFD and the ITTC-57 line become nearly parallel, indicating a closer approximation to pure friction behavior. The second row of the plots shown in Fig. 8 represents the correlation between the form factor and Re (scale factor). The $1 + k$ values have been extracted using the ITT57 friction line and the C_F derived from the CFD simulations, respectively. In this way, the results can be compared with the corresponding EFD data depicted in Fig. 8. The model-scale EFD data have been derived

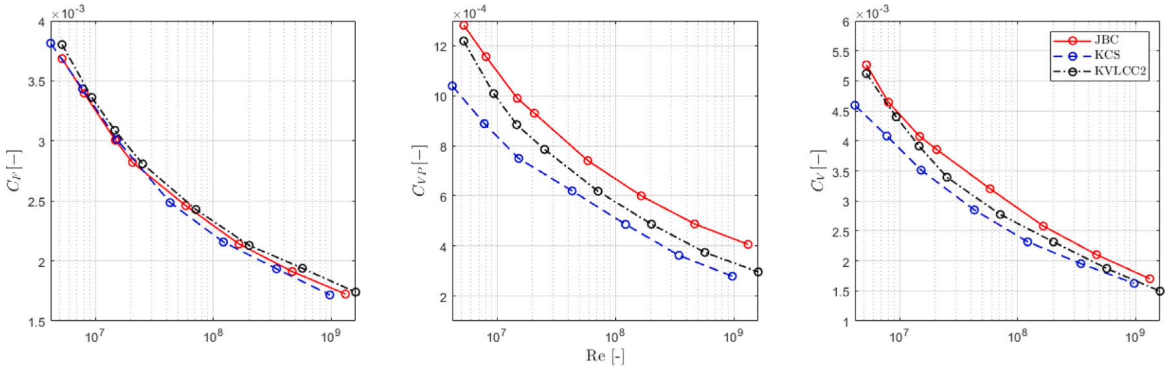

Fig. 7. Variation of C_F (left), C_{PV} (middle) and C_V (right) across scales for JBC, KCS, and KVLCC2.

from Hino et al. (2015) for JBC and Larsson et al. (2010) for KCS and KVLCC2. The $1 + k$ were calculated using Eq. (5), where C_F was derived from CFD simulations (CFD-based form factor) or calculated using the ITTC57 friction line (ITTC57-based form factor). The ITTC57-based form factors show an increasing trend in all test cases, which tend to converge to a constant value when the scaling factor approaches full-scale. On the other hand, CFD-based form factors have a scant impact from scale effect.

The comparison between EFD, ITTC57-based, and CFD-based $1 + k$ values for each hull is presented below:

- **JBC**: CFD-based form factors are periodically increasing by 1.8 % from model to full-scale, while form factors extracted from the friction line ITTC57 perform a slight increase of 3 % from model to full-scale. Their differences from the EFD data are 4.1 and 5.2 in average between model and full scale, respectively.
- **KCS**: Both ITTC57-based and CFD-based results are also slightly increasing from model to full-scale by 1.3 and 1.4 %, respectively. ITTC57-based results show lower discrepancy with EFD data than CFD-based $1 + k$.
- **KVLCC2**: CFD-based results show a constant trend along the range of Re numbers. ITTC57-based results show a linear increment of 5.2 % from model to full-scale with higher divergence from EFD data in full-scale.

The flow behind the transom for the three test cases has been analyzed at scantling draft for both model scale (MS) and full scale (FS), assuming hydrodynamically smooth surfaces without accounting for roughness effects. Fig. 9 shows the normalized axial velocity (u/U) distribution, as well as the in-plane streamlines, on a plane behind the transom ($x/L_{PP} = -0.05$) obtained from the MS and FS simulations including the free surface. The streamlines plotted on these figures show the flow on the yz plane. The lower limit of the normalized velocity has been set to −0.1 to show the forward-moving flow due to the flow separation. These plots reveal a discrepancy between the model and the full-scale axial velocity distribution as well as the effect of the bilge vortex in the propeller plane and the impact of the transom submergence. The model-scale wake is slightly wider and more pronounced relative to the full-scale for all test cases. In the case of KVLCC2, the discrepancy of the wake between model-scale and full-scale is more visible if one observes the streamlines in the transom area, as well as the bigger diameter of the bilge vortex.

6.2. Roughness effect

The results of the systematic variation of the roughness height of the hull surface in FS are also presented in this section. The analysis is carried out for JBC, KCS, and KVLCC2, at $Fr = 0.1$ and Re equal to 1.29×10^9, 9.6×10^8 and 1.57×10^9 in full-scale, respectively. All test cases have been studied in scantling draft. The DB numerical model has been used for the implementation of this analysis. An Average Hull Roughens (AHR) is equally distributed on the entire hull surface for all test cases. A standard hull roughness of $AHR = 150$ μm is used as recommended by ITTC (1978). CFD-based frictional resistance has been used for the 1+k estimation, because the surface roughness effect on C_F must be captured in order to investigate how much it can affect the $1+k$ prediction. Moreover, two more AHRs have been included to study the form factor sensitivity on surface roughness variation. As seen in Fig. 10, the numerically calculated resistance components increase as the AHR increases. Comparing the results between the roughness heights of 150 μm and 250 μm, C_F and C_{PV} the results increase approximately by 9 % and 7.5 %, respectively, while C_V shows an increase of about 8.5 %. On the other hand, comparing the smooth hull surface with hull roughness of 150 μm, the increase is steeper, which means that the resistance coefficients are more sensitive in lower AHR values.

The dependency of the form factor on the surface roughness height is presented in Fig. 11, where CFD-based and EFD-based data (Hino et al., 2015; Larsson and Raven, 2010) are added for comparison. The same strongly increasing trend is observed for KCS and KVLCC2, while gradual increase is noticed for JBC. The form factor shows an increasing trend of 1.5 %, 2.8 % and 3.2 % for JBC, KCS and KVLCC2, respectively, within the studied variation range of AHR. Results for higher ARH, that is 300–500 μm, are not presented in this study, because negligible variation of resistance components and form factor is observed. This happens because the ARH is larger than the height of the wall-adjacent cell, $R^+ > y^+$. In this case, Simcenter STAR-CCM+ restricts the local roughness height by making it the same as the cell height, $R^+ = y^+$. Wall roughness can be modeled without using this limiter by deactivating the wall roughness parameter at the boundary, but, in this case, it decreases the accuracy of the simulation.

The wake distribution for the same test cases and two different AHR values as well as the smooth hull is illustrated in Fig. 12. Fr and Re are the same as stated above. It can be concluded that the wake is not strongly dependent on the change in AHR, but a minor thickening of the nominal wake can be noticed for increases in AHR. The wake around the skeg, where the boundary layer thickness is the maximum, shows the greatest sensitivity to changes in the roughness height. This can be a consequence of the flow with lower momentum, which is more prone to change due to the increased shear stresses in this region.

6.3. Transom submergence effect

Variation in transom submergence significantly affects total resistance and constitutes an important part of the 2–k method. Therefore, this study systematically investigates the influence of transom submergence on the local flow characteristics behind the transom through variation of the draft. Table 7 shows the form factors obtained

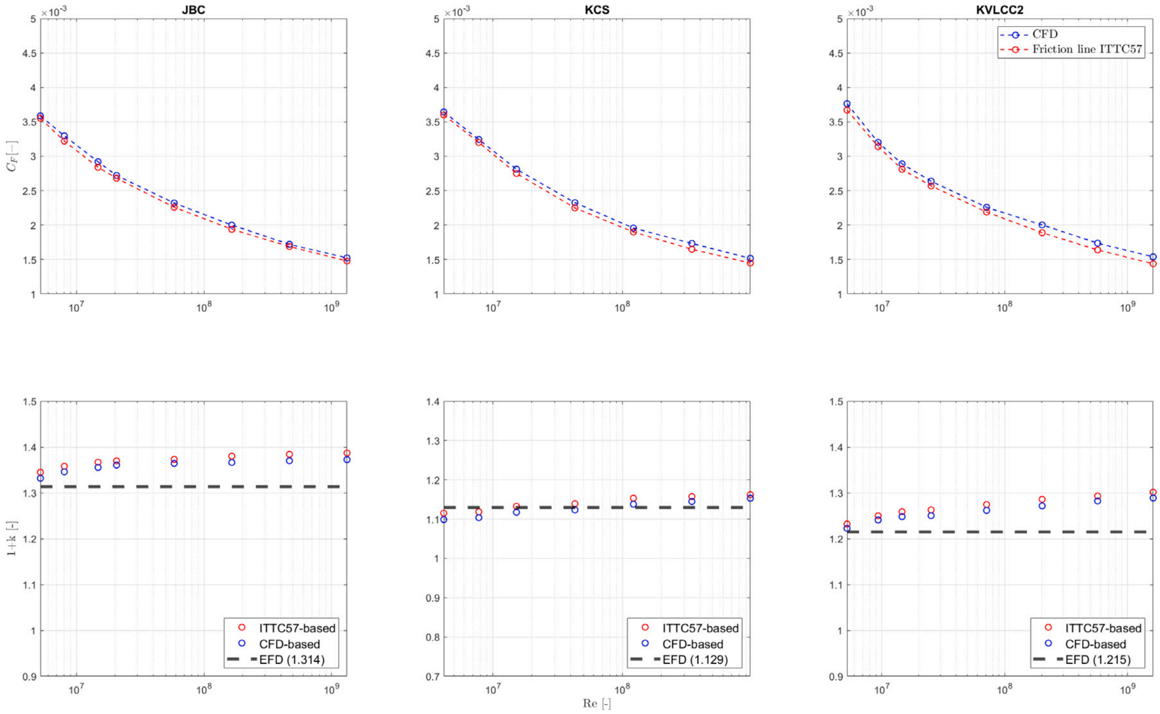

Fig. 8. Correlation between ITTC57 friction line and CFD (DB) frictional resistance coefficient (top), and 1+k variation (bottom) in different Re and scantling draft using DB model.

Table 7
Corrections using two form factor (2-k) method for JBC, KCS, KVLCC2, 180K DWT BC and 82K DWT BC at different drafts.

Test case	T [m]	T_{tr} [m]	y_{tr} [m]	A_{tr} [m^2]	A_{max} [m^2]	tr_{ra} [–]	$tr_{fullness}$ [–]	Fr_{tr} [–]	k_{tr} (Eq. (10)) [–]	k_M (CFD) [–]	$k_S = k_M + k_{tr}$ (CFD-transom corr.) [–]
JBC	16.5	1.16	3.94	5.16	1124.00	0.005	0.564	0.248	0.00000	0.335	0.335
	17.0	1.66	5.40	9.83	1124.00	0.009	0.548	0.207	0.00000	0.337	0.337
	17.5	2.16	6.78	15.93	1124.00	0.014	0.544	0.182	0.00000	0.340	0.340
	18.0	2.66	8.01	23.34	1124.00	0.208	0.548	0.164	0.00071	0.344	0.344
	18.5	3.16	9.04	31.89	1124.00	0.029	0.558	0.150	0.00551	0.351	0.356
	19.0	3.66	9.92	41.39	1124.00	0.037	0.570	0.139	0.01137	0.361	0.372
KCS	12.0	0.70	9.01	7.80	380.85	0.0205	0.619	0.418	0.00391	0.100	0.104
	13.0	1.70	12.98	30.36	413.05	0.0735	0.688	0.268	0.05868	0.102	0.161
	14.0	2.70	14.65	58.19	445.26	0.131	0.736	0.213	0.13144	0.105	0.236
	15.0	3.70	15.50	88.44	477.46	0.185	0.771	0.182	0.20700	0.109	0.316
	16.0	4.70	15.94	119.93	509.69	0.235	0.801	0.161	0.27500	0.114	0.389
	17.0	5.70	16.10	152.00	541.86	0.281	0.828	0.147	0.33260	0.119	0.452
KVLCC2	20.8	2.00	5.88	13.71	342.52	0.040	0.583	1.275	0.01343	0.252	0.265
	21.8	3.00	7.28	26.93	342.52	0.079	0.617	1.041	0.04460	0.255	0.299
	22.8	4.00	8.10	42.38	342.52	0.124	0.654	0.902	0.08147	0.259	0.341
	23.8	5.00	8.58	59.12	342.52	0.173	0.689	0.806	0.10200	0.262	0.364
180K DWT BC	16.0	2.00	4.04	8.72	718.44	0.012	0.540	1.200	0.00000	0.239	0.239
	17.0	3.00	5.43	18.25	763.44	0.024	0.560	0.979	0.00153	0.253	0.255
	18.3	4.30	6.79	34.23	821.94	0.042	0.586	0.818	0.00504	0.261	0.266
82K DWT BC	12.2	0.97	4.81	6.01	392.32	0.002	0.644	0.226	0.00000	0.252	0.252
	13.0	1.77	6.31	15.03	418.18	0.036	0.673	0.168	0.00847	0.262	0.271
	14.0	2.77	7.24	28.71	450.40	0.064	0.716	0.134	0.02900	0.278	0.307
	15.0	3.77	7.32	43.00	482.65	0.089	0.779	0.115	0.05176	0.292	0.344

from the full-scale CFD simulations, including the transom submergence correction formula, Eq. (10). The benchmark hulls including JBC, KCS, KVLCC2, and the two commercial hulls have been chosen for this systematic analysis. The two commercial hulls are selected since model test results are available from the FORCE Technology's database (FORCE, 2021a,b).

The analysis is conducted at four different Froude numbers, $Fr = 0.1, 0.2, 0.3, 0.4$, for both model-scale (Fig. 13) and full-scale (Fig. 14) conditions, considering both smooth and rough hull surfaces (with an average hull roughness, ($AHR = 150$ μm), using the free-surface (F-S) simulation approach. Additionally, the Prohaska method is employed to estimate the resistance ratios C_{Tm}/C_{Fm} and C_{Ts}/C_{Fs} at model- and full-scale, respectively. The frictional resistance coefficients are derived directly from the CFD simulations. As illustrated in Fig. 13, the CFD results display consistent trends across different drafts, with no notable variations observed—this consistency also applies to the two bulk carrier hulls analyzed. For the JBC hull, simulations using the

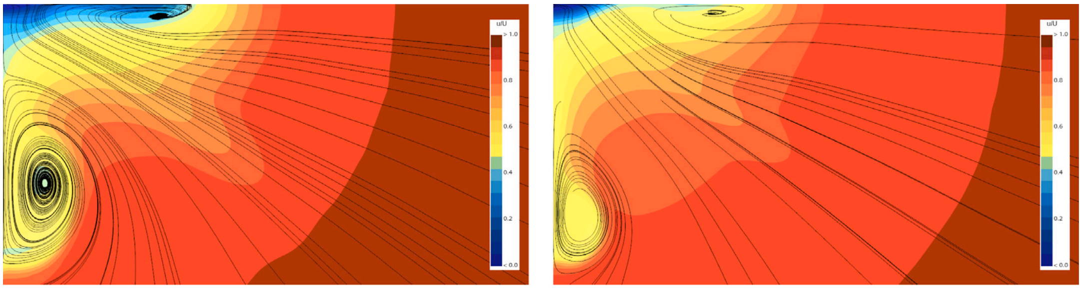

(a) JBC (MS) / $Re = 1.70 \times 10^5$ (b) JBC (FS) / $Re = 1.29 \times 10^9$

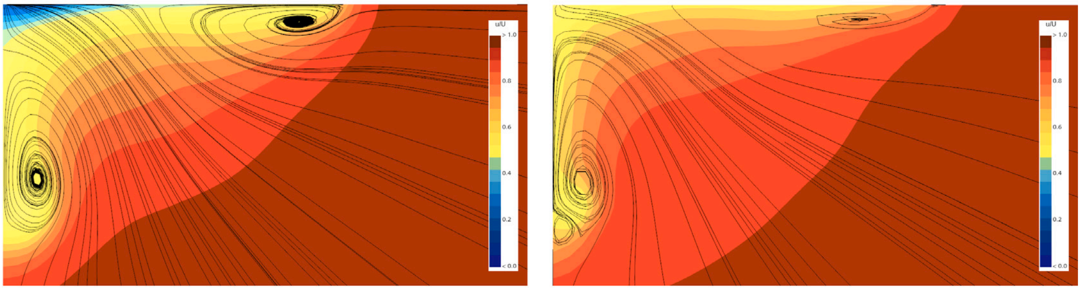

(c) KCS (MS) / $Re = 3.87 \times 10^5$ (d) KCS (FS) / $Re = 9.60 \times 10^8$

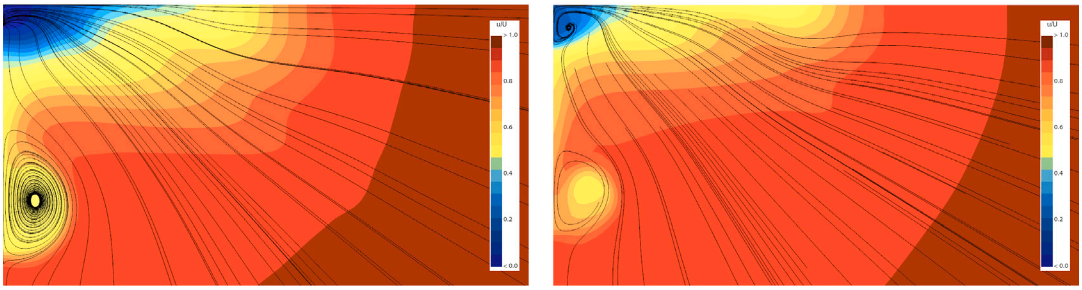

(e) KVLCC2 (MS) / $Re = 4.77 \times 10^5$ (f) KVLCC2 (FS) / $Re = 1.57 \times 10^9$

Fig. 9. Normalized axial velocity of the wake with in-plane arrows indicating flow direction for the scantling draft at $x/L_{PP} = -0.05$ and $Fn = 0.1$ in both MS and FS (DB, $k-\omega$ model, AHR = 0).

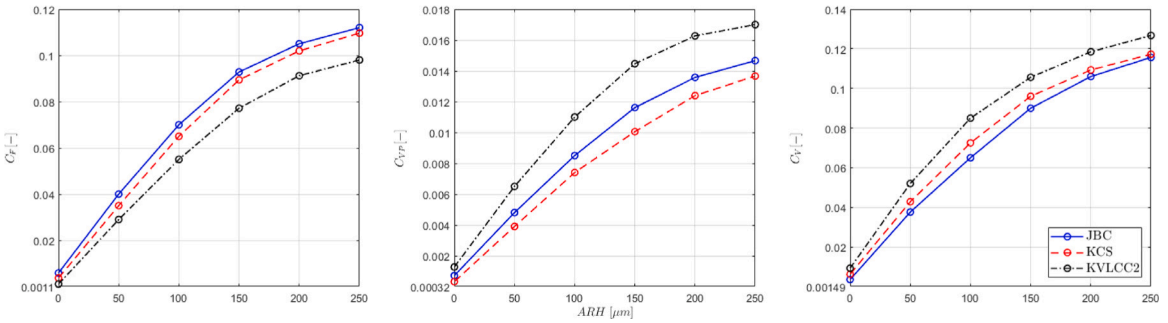

Fig. 10. Effect of roughness height variation on C_F, C_{PV} and C_V for JBC, KCS and KVLCC2 in FS.

double-body (DB) model have also been performed, enabling a direct comparison with the corresponding F-S results.

In Fig. 13, the results extracted from the JBC test case are shown. The plotted k trendlines are almost parallel to each other, and the values increase as the draft increases. This is considered reasonable because the draft increases as the transom is immersed, creating a more pronounced recirculation water region in its wake, directly influencing the predicted form factors. The trendlines of the two higher drafts and for $Fr^4/C_{Fm} > 0.016$ approach each other, which might be due to the uncertainty of the results created by the unstable and highly turbulent flow behind the transom. For the 180K DWT and 82K DWT hulls, extra simulations have been carried out for each of the studied drafts so that the CFD results correspond to the EFD ones.

By examining the y-intercept of the C_{Tm}/C_{Fm} ratio at the scantling draft, as determined via the Prohaska method, and comparing it with the corresponding experimental fluid dynamics (EFD) data, discrepancies of less than 2 % for the 180K DWT and 4.5 % for the 82K DWT bulk carriers are observed. Although the EFD trends differ between the two test cases—and notable scatter is present in the EFD results for the 82K DWT case—the CFD predictions remain in reasonable agreement with the experimental data. Nevertheless, the CFD results for the 180K DWT case exhibit noticeable scatter within the range

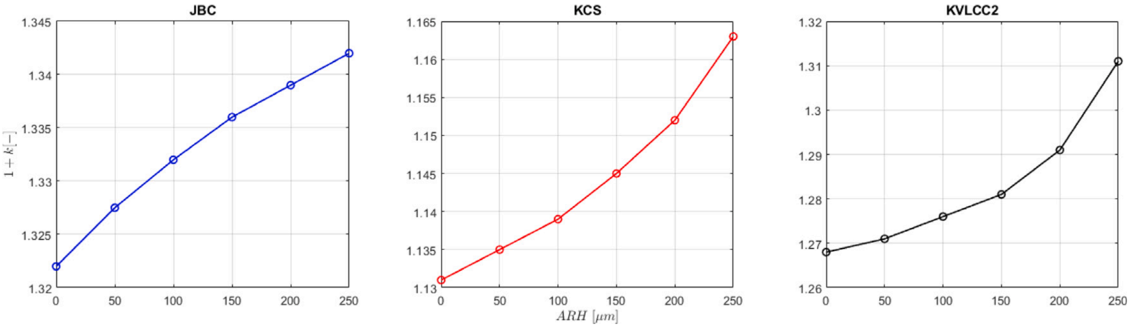

Fig. 11. 1+k sensitivity to AHR variation for three benchmark hulls.

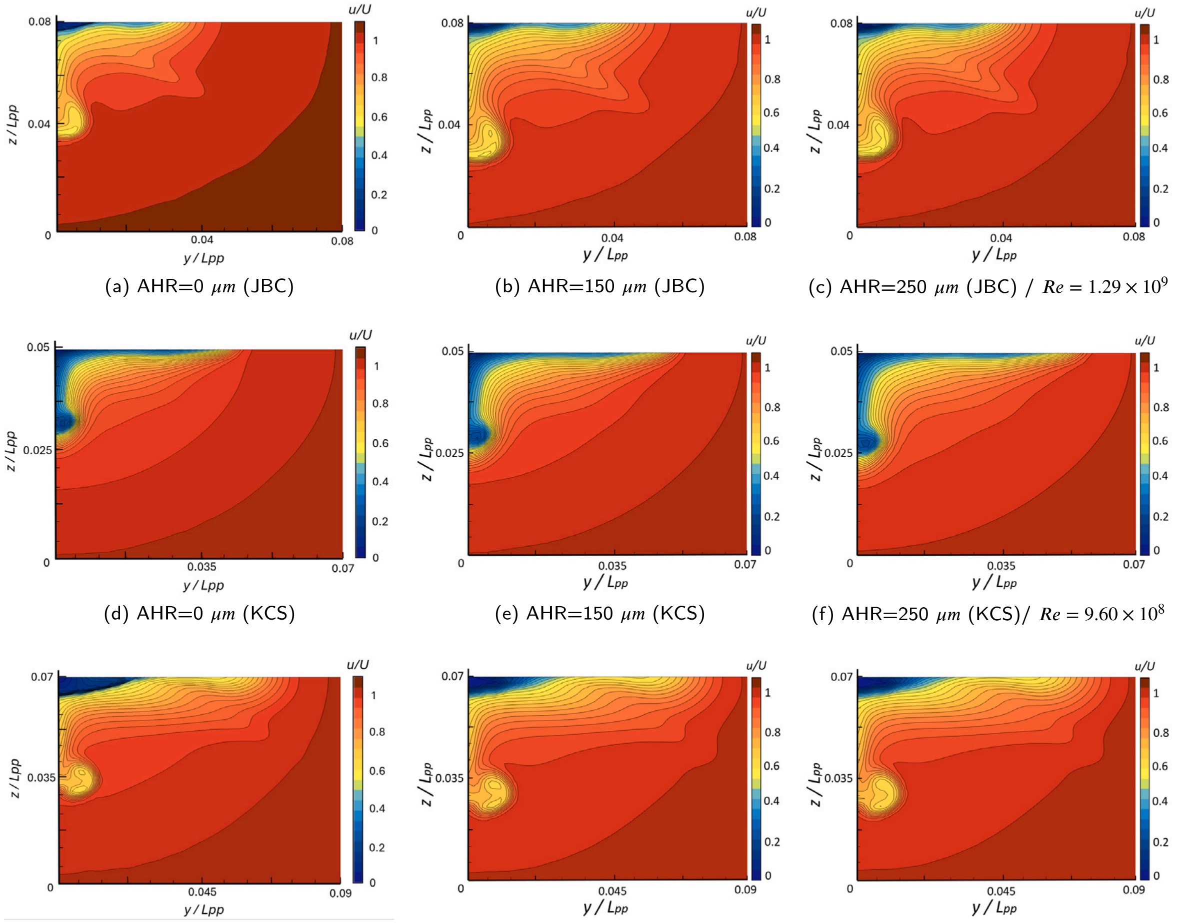

(a) AHR=0 μm (JBC)

(b) AHR=150 μm (JBC)

(c) AHR=250 μm (JBC) / $Re = 1.29 \times 10^9$

(d) AHR=0 μm (KCS)

(e) AHR=150 μm (KCS)

(f) AHR=250 μm (KCS)/ $Re = 9.60 \times 10^8$

(g) AHR=0 μm (KVLCC2)

(h) AHR=150 μm (KVLCC2)

(i) AHR=250 μm (KVLCC2)/ $Re = 1.57 \times 10^9$

Fig. 12. Normalized velocity of the wake for three benchmark hulls at $x/L_{PP} = -0.05$ for T_s and $Fr = 0.1$ in FS for smooth hull and two AHR values (DB, $k-\omega$ model).

$0.005 < Fr^4/C_{Fm} < 0.02$. This variation is attributed to the inherent difficulties in achieving numerical convergence of frictional and viscous pressure resistance components at very low speeds when using the free-surface (F-S) modeling approach.

As shown in Fig. 14, the results from the systematic variation of transom submergence at full scale exhibit consistent behavior, resulting in a narrow range of y-intercept values—particularly evident in the JBC test case. The trendlines of the CFD data intersect at approximately $Fr^4/C_{Fs} > 0.03$, leading to differing slopes among the cases. In full-scale (FS) simulations that account for free-surface elevation, the ratio C_{Ts}/C_{Fs} becomes sensitive to the wave resistance component, which contributes to the overall resistance. Although wave elevation remains relatively low at small Froude numbers, it still influences the total-to-frictional resistance ratio and, consequently, the interpretation of the results.

Comparison of y-intercept between model-scale and full-scale shows that broader range of C_{Tm}/C_{Fm} values is observed in full-scale than in model-scale for 180K DWT BC and 82K DWT BC among the studied drafts. In case of JBC, asymptotic values in full-scale cover a narrower range of the C_{Tm}/C_{Fm} ratio.

Tables 8–10 show the results on the form factor prediction for all test cases in both the model and the full-scale and both numerical

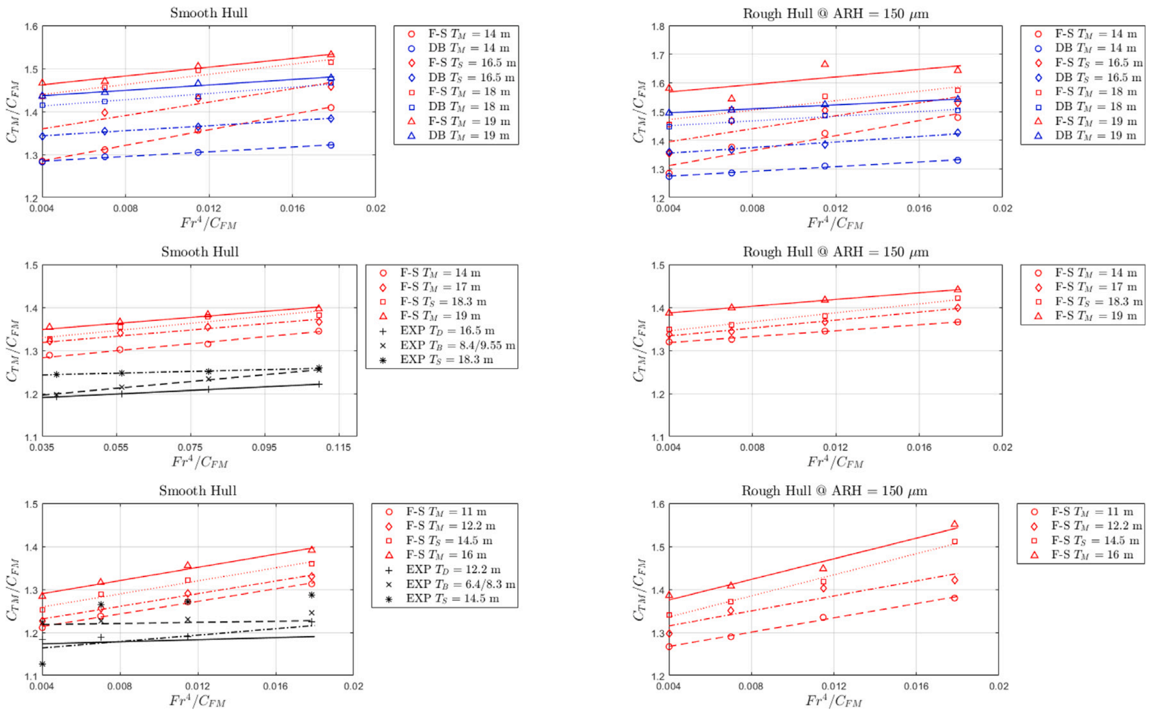

Fig. 13. Dependence of C_{Tm}/C_{Fm} on the variation of the draft in model-scale for smooth and rough hull surfaces by using the Prohaska method and F-S model. JBC (top), 180K DWT BC (middle), 82K DWT BC (bottom).

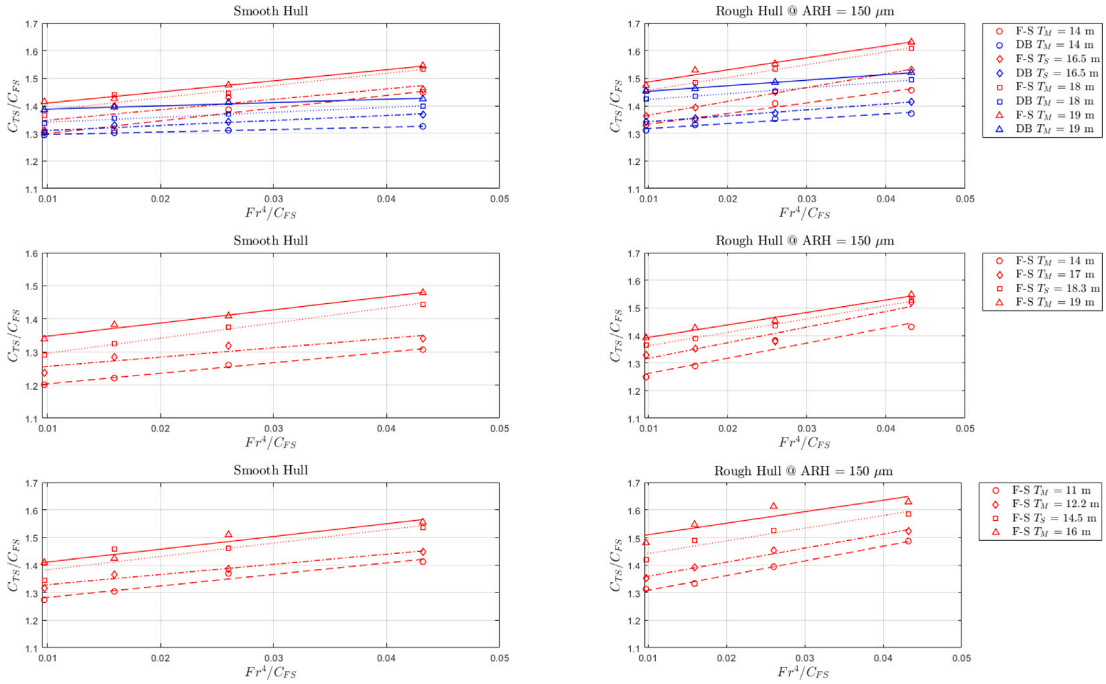

Fig. 14. Dependence of C_{Tm}/C_{Fm} on the variation of the draft in full-scale for smooth and rough hull surfaces by using the Prohaska method and F-S model. JBC (top), 180K DWT BC (middle), 82K DWT BC (bottom).

Table 8

Comparison of 1+k results with data from the literature in model-scale and full-scale using CFD-based frictional resistance and the DB model. All results correspond to scantling draft.

Test case	CFD		2-k method	EFD	CFD vs. EFD		CFD MS vs. CFD FS	2-k vs. EFD
	MS	FS			MS	FS		
JBC	1.312	1.322	1.335	1.314 (Hino et al., 2015)	0.23 %	0.61 %	3.92 %	1.50 %
KCS	1.090	1.131	1.109	1.129 (Larsson and Raven, 2010)	3.45 %	0.18 %	3.63 %	1.77 %
KVLCC2	1.257	1.268	1.234	1.215 (Larsson and Raven, 2010)	2.38 %	3.23 %	0.87 %	1.20 %
DTMB 5415	1.134	1.215	1.138	1.120 (Larsson and Raven, 2010)	1.27 %	2.72 %	6.67 %	1.58 %
ONRT	1.107	1.174	1.145	–	–	–	5.71 %	–
180K DWT BC	1.231	1.202	1.195	1.182 (FORCE, 2021a)	2.92 %	1.66 %	2.36 %	1.09 %
82K DWT BC	1.252	1.247	1.252	1.262 (FORCE, 2021a)	0.79 %	0.12 %	0.40 %	0.82 %

models. The comparison errors of the CFD and EFD form factors shown in these two tables are obtained through Eq. (29).

$$\Delta k = \frac{k_{CFD} - k_{EFD}}{k_{CFD}} \times 100\ [\%] \tag{29}$$

Experimental data are extracted from Hino et al. (2015) (JBC), Larsson et al. (2010) (KCS, KVLCC2 and DTMB 5415), FORCE (2021a) (180K DWT BC) and FORCE (2021a) (82K DWT BC). Mandru and Pacuraru (2021) does not provide information on the form factor or the estimate of the friction resistance, therefore the comparison between the CFD and EFD results for ONRT is not included. Tables 8 and 9 show the discrepancies between the CFD-based 1+k estimation and the EFD results using CFD-based frictional resistance and ITTC57 friction line, respectively. Results indicate that the 2−k method gives better approximation between CFD and EFD data in both cases than the results from DB in model and full scale. However, when the ITTC 57 friction line is used, the 2−k method gives even closer 1+k values to the EFD data. This can justify the improved 1+k estimation using the 2−k method.

Fig. 15 shows the form factor of JBC, KCS, and KVLCC2, as well as the two commercial vessels for different transom submergence. The results are obtained from CFD-based model-scale, full-scale simulations, and full-scale simulations using the transom submergence correction formula and they are also presented in Table 7. The resulting form factors are based on CFD-based C_F. A difference of less than 5.0 % is observed for all test cases except KCS. In this case, the discrepancy between CFD-based estimate in model and full-scale with the form factors extracted using the empirical formula of the 2−k method, Eq. (10), is 5.1 % and 6.7 % for drafts 16.0 and 17.0 m, respectively. KCS is the only container ship studied in this analysis, whereas the other test cases include three bulk carriers and a tanker. Specifically, the shape of the KCS hull, particularly its stern, differs compared to the rest of the test cases, as it has a larger wetted transom area. This leads to more intense recirculation and turbulence in the wake of the transom, resulting in a more significant impact on form resistance, that is, C_{VP}. Hence, C_{VP} is increasing sharply, while CF remains relatively similar, resulting in increased form factor and the form factor in full-scale CFD simulations. Generally, the form factor is sensitive to the wetted transom area and larger transom areas result in a higher form factor, indicating greater flow separation and energy loss in the wake of the ship and thus higher resistance.

7. Conclusions and future work

This paper presents a systematic CFD and V&V investigation of form-factor estimation that extends the two-form-factor (2−k) methodology to five benchmark and two commercial hulls compares double-body and free-surface RANS at both model and full scale with quantified grid and modeling uncertainty, provides a comprehensive sensitivity analysis to hull roughness (AHR = 0–250 μm) and draft/transom submergence, and demonstrates that applying the 2−k correction reduces full-scale extrapolation errors for hulls with wetted transoms. The combined DFBI/VoF full-scale simulations and the grid-refinement asymptotic analysis give practical modeling guidance for reliable CFD-based form-factor estimation.

1. The present study extends the application of the two-form-factor (2−k) methodology to a broader set of hull geometries than previously reported, including five benchmark hulls and two commercial vessels. This systematic multi-hull investigation confirms the method’s robustness across diverse form characteristics and validates its applicability beyond the limited case sets examined in earlier studies.
2. A rigorous verification and validation (V&V) procedure was performed for both double-body and free-surface RANS simulations at model and full scale, including grid-refinement analyses and quantified numerical uncertainties. The results demonstrate strong consistency between CFD predictions and available experimental data, thereby establishing reliable numerical requirements for form-factor estimation.
3. The sensitivity of the form factor to hull-surface roughness was quantified through a controlled AHR variation study, showing that increases in roughness height lead to systematic increases in frictional and viscous pressure resistance components. The analysis also identifies the practical limitations of wall-roughness modeling at high AHR values, offering guidance for accurate roughness representation in CFD-based form-factor assessments.
4. A detailed investigation of draft variation and transom submergence demonstrates that the CFD-derived transom contribution aligns closely with the empirical correction proposed in the 2−k formulation. The comparison across multiple hull forms clarifies the range of validity of the transom-correction model and highlights cases where CFD provides enhanced predictive capability.
5. The combined CFD–EFD analysis shows that the 2−k approach systematically improves the agreement between model- and full-scale resistance predictions, particularly for hulls with wetted transoms. This confirms that the 2−k method enhances the reliability of viscous-resistance extrapolation and provides a practical improvement over conventional ITTC-78 form-factor procedures.

Future work should extend the $2 - k$ methodology to a wider range of hull forms and appendage configurations to further assess its generality across more complex geometries. In parallel, enhanced roughness-modeling strategies are needed, particularly for higher AHR values where current wall-function limitations constrain accuracy. Future studies should, therefore, explore alternative roughness formulations and adaptive meshing approaches. Finally, dedicated experiments focusing on varying drafts and transom-submergence conditions would provide high-quality data for validating the transom-related contributions within the $2 - k$ framework and strengthening its empirical foundation.

CRediT authorship contribution statement

Minas Argyros: Writing – review & editing, Writing – original draft, Visualization, Validation, Methodology, Investigation, Formal

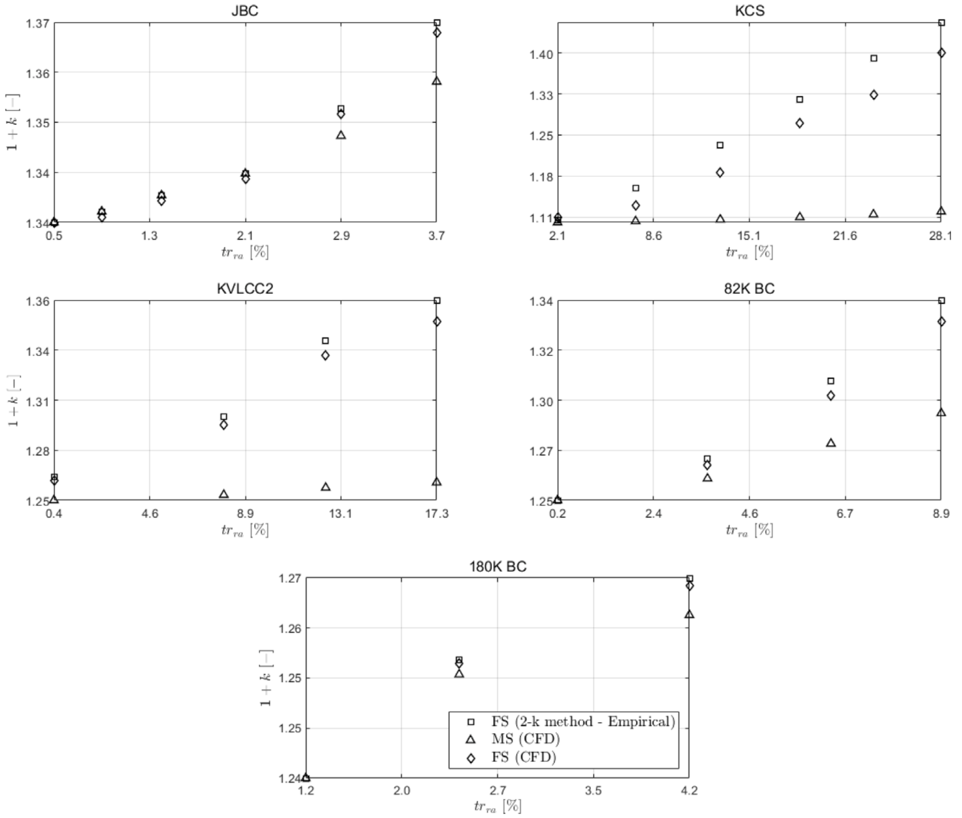

Fig. 15. Sensitivity of 1+k under transom submergence variation for all test cases in model scale, full scale and using the 2−k method.

Table 9
Comparison of 1+k results with data from the literature in model-scale and full-scale using ITTC57 friction line and the DB model. All results correspond to scantling draft.

Test case	CFD		2-k method	EFD	CFD vs. EFD		CFD MS vs. CFD FS	2-k vs. EFD
	MS	FS			MS	FS		
JBC	1.341	1.345	1.322	1.314 (Hino et al., 2015)	2.01 %	2.30 %	0.30 %	0.61 %
KCS	1.112	1.118	1.131	1.129 (Larsson and Raven, 2010)	0.79 %	0.97 %	0.51 %	0.18 %
KVLCC2	1.228	1.235	1.221	1.215 (Larsson and Raven, 2010)	3.43 %	3.55 %	0.52 %	0.65 %
DTMB 5415	1.090	1.093	1.10	1.120 (Larsson and Raven, 2010)	2.65 %	2.41 %	0.27 %	0.18 %
ONRT	1.109	1.115	1.117	–	–	–	5.71 %	–
180K DWT BC	1.125	1.135	1.175	1.182 (FORCE, 2021a)	4.82 %	3.98 %	0.88 %	0.59 %
82K DWT BC	1.208	1.215	1.296	1.262 (FORCE, 2021a)	4.28 %	3.72 %	0.58 %	0.55 %

Table 10
Comparison of 1+k results with data from the literature in model-scale and full-scale using CFD-based frictional resistance and the F-S model. All results correspond to scantling draft.

Test case	CFD		2-k method	EFD	CFD vs. EFD		CFD MS vs. CFD FS	2-k vs. EFD
	MS	FS			MS	FS		
JBC	1.307	1.321	1.334	1.314 (Hino et al., 2015)	0.53 %	0.53 %	1.06 %	1.50 %
KCS	1.093	1.129	1.107	1.130 (Larsson and Raven, 2010)	3.19 %	0.09 %	3.27 %	1.95 %
KVLCC2	1.261	1.272	1.232	1.215 (Larsson and Raven, 2010)	3.65 %	4.48 %	0.86 %	1.38 %
DTMB 5415	1.131	1.211	1.139	1.120 (Larsson and Raven, 2010)	0.97 %	7.51 %	6.61 %	1.67 %
ONRT	1.104	1.175	1.142	–	–	–	6.04 %	–
180K DWT BC	1.235	1.198	1.197	1.182 (FORCE, 2021a)	4.29 %	1.34 %	3.00 %	1.25 %
82K DWT BC	1.249	1.251	1.255	1.262 (FORCE, 2021a)	1.03 %	0.87 %	0.16 %	0.55 %

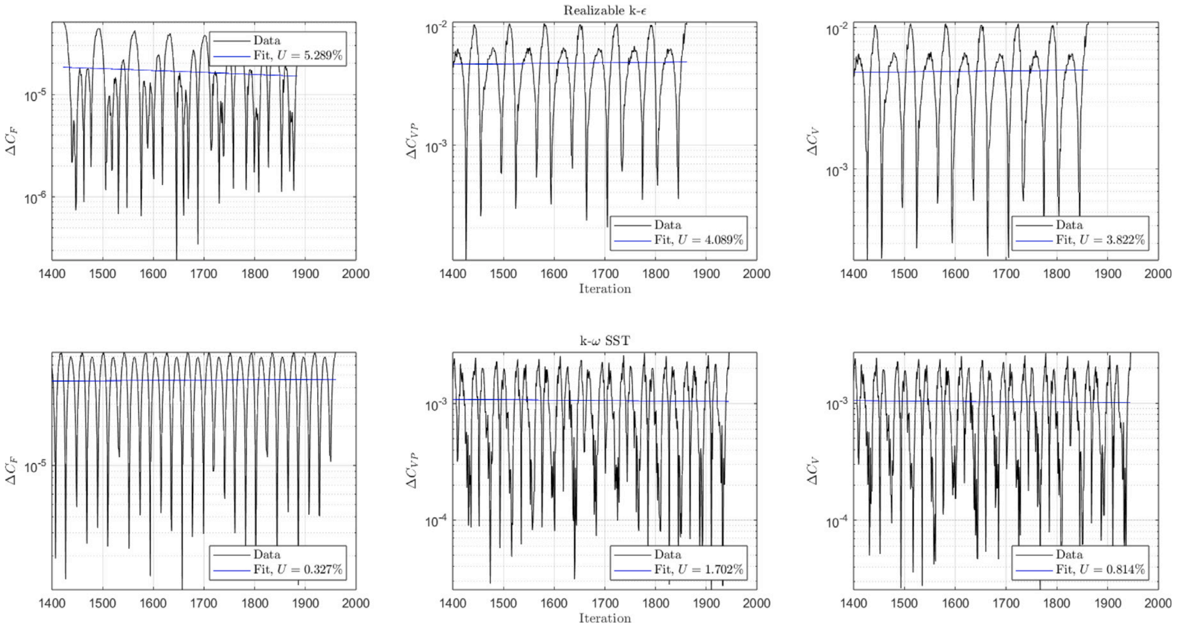

Fig. A.1. Iterative error of C_F for k − ω SST and realizable k − ϵ models in MS using the DB approach.

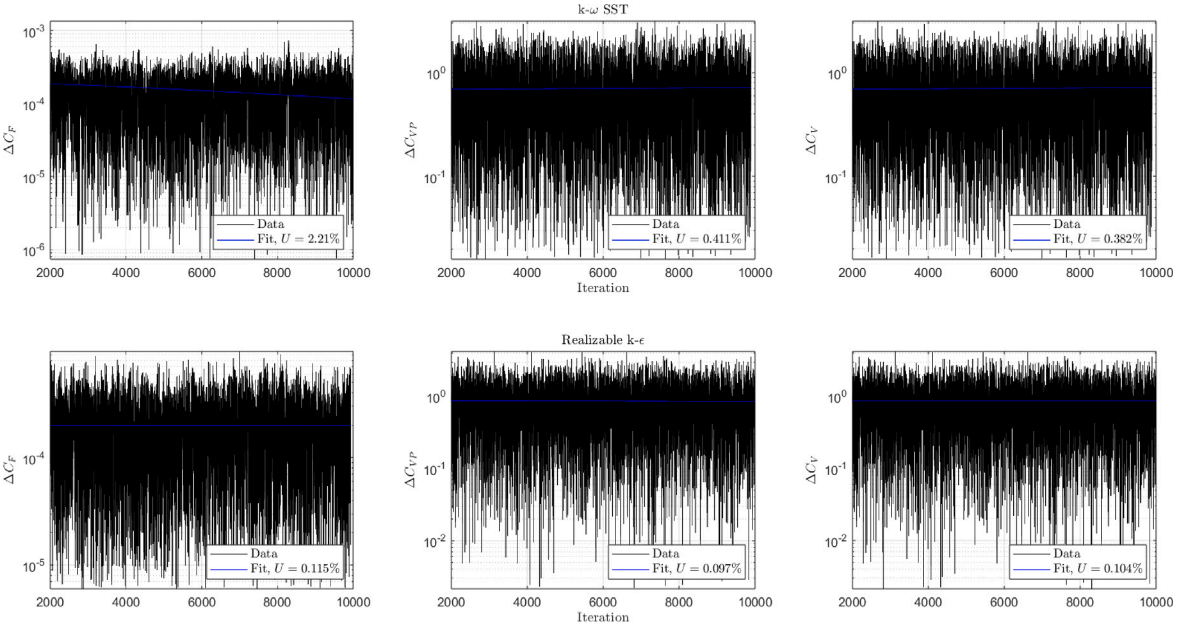

Fig. A.2. Iterative error of C_F for k − ω SST and Realizable k − ϵ models in FS using the DB approach.

analysis, Data curation. **Simone Mancini:** Writing – review & editing, Supervision, Methodology, Conceptualization. **Kadir Burak Korkmaz:** Writing – review & editing, Validation, Methodology. **Arash Eslamdoost:** Writing – review & editing, Supervision, Methodology, Conceptualization.

Declaration of competing interest

The authors declare that they have no known competing financial interests or personal relationships that could have appeared to influence the work reported in this paper.

Acknowledgments

This research was partially financed by the Ministry of Higher Education and Science, Performance Contract Programme 2021–2024 Activity FT03.01 and the computational resources provided by FORCE Technology. The funders were not involved in any aspect of the study, including its design, data collection, analysis, or interpretation, the writing of the manuscript, or the decision to publish the findings.

Appendix. C_F iterative error

The iterative errors of C_F in MS and FS are presented in Figs. A.1 and A.2, respectively. The selection of C_F for the study of iterative error is made because it constitutes the main factor for the estimation of the form factor, as has been mentioned above. In the case of MS, 2000 iterations have been selected, whereas 10 000 iterations are applied for the FS simulations. Observing Fig. A.1, the simulations are completed before they reach the entire 2000th iteration, which means that the results converge relatively rapidly. Moreover, the first 1400 (MS) and

2000 (FS) iterations have been removed from the graphical depiction because the intensive oscillations at the beginning of the simulation are not of high interest for the prediction of iterative error. Therefore, the illustrated fit curves have a linear trend and represent the average value of the error.

Data availability

Data related to the two commercial hulls are confidential. Data related to the benchmark hulls will be made available on request.

References

Cebeci, T., Bradsaw, P., 1977. Momentum Transfer in Boundary Layers. Hemisphere Publishing/McGraw-Hill, pp. 176–180.

19th Committe ITTC, 1990. Report of the resistance and flow committee. In: International Towing Tank Conference.

Dogrul, A., Song, S., Demirel, Y.K., 2020. Scale effect on ship resistance components and form factor. Ocean Eng. http://dx.doi.org/10.1016/j.oceaneng.2020.107428, Elsevier.

Eca, L., Hoekstra, M., 2014. A procedure for the estimation of the numerical uncertainty of cfd calculations based on grid refinement studies. J. Comput. Phys. 262, 104–130. http://dx.doi.org/10.1016/j.jcp.2014.01.006.

FORCE, T., 2021a. 121-29152 energy saving devices analysis for a 180k dwt bulk carrier.

FORCE, T., 2021b. 121-30654 energy saving devices analysis for a 82k dwt bulk carrier.

Hino, T., Stern, F., Larsson, L.M.V., Hirata, N., Kim, J., 2015. Numerical Ship Hydrodynamics, An Assessment of the Tokyo 2015 Workshop. Vol. 94, Springer, ISBN: 978-3-030-47571-0, URL: https://link.springer.com/book/10.1007/978-3-030-47572-7.

Hughes, G., 1954. Friction and form resistance in turbulent flow, and a proposed formulation for use in model and ship correlation. R.I.N.A. 96.

ITTC, 1957. Subjects 2 and 4 skin friction and turbulence stimulation.

ITTC, 1978. Report of performance committee. URL: https://www.marin.nl/en/research/free-resources/verification-and-validation/verification-tools.

ITTC, 2008. Uncertainty Analysis in Cfd Verification and Validation Methodology and Procedures. Recommended Procedures and Guidelines, 7.5-03-01-01, Rev 02. URL: https://ittc.info/media/4184/75-03-01-01.pdf.

Ji-Woo, H., Rafat, I.A.S., Byoung-Kwon, A., Se-Myun, O.D.H.L., 2024. Ldv measurements of boundary layer velocity profiles on flat plates with different surface roughnesses. Int. J. Nav. Archit. Ocean Eng. 16, 100619, Science Direct. URL: https://doi.org/10.1016/j.ijnaoe.2024.100619.

Korkmaz, K., Werner, S., Bensow, R., 2021a. Verification and validation of cfd based form factors as a combined cfd/efd method. J. Mar. Sci. Eng. 9, 75, URL: https://doi.org/10.3390/jmse9010075.

Korkmaz, K., Werner, S., Bensow, R., 2022. Scaling of wetted-transom resistance for improved full-scale ship performance predictions. Ocean Eng. 226, Elsevier. URL: https://doi.org/10.1016/j.oceaneng.2022.112590.

Korkmaz, K., Werner, S., Sakamoto, N., Queutey, P., Deng, G., Yuling, G., Guoxiang, D., Maki, K.Y.H., Akinturk, A., Sayeed, T., Hino, T., Zhao, F., Tezdogan, T., Demirel, Y., Bensow, R., 2021b. Cfd-based form factor determination method. Ocean Eng. 220, Elsevier. URL: https://doi.org/10.1016/j.oceaneng.2020.108451.

Kuiquan, D., Qingbo, L., Yanxin, L., Han, J., Shuang, W., Manxia, Z., 2024. Data-driven approach to evaluate the impact of hull roughness on main engine load of river-sea ships. Ocean Eng. 312 (Part 2), 119239, Science Direct. URL: https://doi.org/10.1016/j.oceaneng.2024.119239.

Larsson, L., Raven, C.H., 2010. Ship and Resistance Flow. In: Principles of Naval Architecture Series, SNAME, USA, ISBN: 978-0-939773-76-3.

Larsson, L., Stern, F., Visonneua, M., 2010. Gothenburg 2010: A Workshop on Numerical Ship Hydrodynamics. Proceedings. Report No. R-10:122, Vol. II, ISSN No. 1652-9189.

Lopes, R., Eslamdoost, A., Johansson, R., RoyChoudhury, S., Bensow, R.E., Hogström, P., Ponkratov, D., 2025. Resistance prediction using cfd at model- and full-scale and comparison with measurements. Ocean Eng. 321, URL: https://doi.org/10.1016/j.oceaneng.2025.120367.

Mandru, A., Pacuraru, F., 2021. The effect of appendages on ship resistance. IOP Conf. Ser.: Mater. Sci. Eng. http://dx.doi.org/10.1088/1757-899X/1182/1/012041.

MARIN, 2022. URL: https://www.marin.nl/en/research/free-resources/verification-and-validation/verification-tools. verification Tools from MARIN.

Mikkelsen, H., Steffensen, L., Ciortan, C., Walther, J.H., 2019. Ship scale validation of cfd model of selfpropelled ship. In: Bensow, R., Ringsberg, J. (Eds.), MARINE 2019 Computational Methods in Marine Engineering VIII. International Center for Numerical Methods in Engineering.

Minchang, K., Jeonghwa, S., Min-a, K., Myoung-soo, K., Dong-Hwan, K.J.P., Woochan, S., 2025. Examination of wave pattern resistance estimation method by experiments and numerical analyses. Int. J. Nav. Archit. Ocean Eng. 17, 100679, Science Direct. URL: https://doi.org/10.1016/j.ijnaoe.2025.100679.

Otzen, J.F., 2010. Uncertainty Assessment for Kcs Resistance and Propulsion Tests in Waves. Lyngby, Denmark.

Prohaska, C., 1966. A simple method for the evaluation of the form factor and low speed wave resistance. In: Proceeding of 11th ITTC.

Quintuña, M., Horn, P., Zhang, J., Sprenger, F., 2024. Combined Efd and Cfd Approach for Full Scale Ship Resistance Predictions using the Form Factor. The American Society of Mechanical Engineers, http://dx.doi.org/10.1115/OMAE2024-126397.

Simman, 2008. 2008 Workshop Verification and Validation of Ship Manoeuvring Simulation Methods. URL: http://www.simman2008.dk/KVLCC/KVLCC2/kvlcc2_geometry.html.

STAR-CCM+, S., 2023. Siemens software. URL: https://plm.sw.siemens.com/en-US/simcenter/fluids-thermal-simulation/star-ccm/.

Stern, F., Wilson, R., Coleman, H., Paterson, E., 2021. Comprehensive approach to verification and validation of cfd simulations—part 1: Methodology and procedures. J. Fluids Eng. 123, 793–802, 2001. and ITTC 75-03-01-01 Rev 04 Recommended Procedures and Guidelines Uncertainty Analysis. ITTC: Zürich, Switzerland.

Terziev, M., Tezdogan, T., Demirel, Y.K., Villa, D., Mizzi, S., Incecik, A., 2021. Exploring the effects of speed and scale on a ship's form factor using cfd. Int. J. Nav. Archit. Ocean Eng. Science Direct. 2092-6782/© 2021 Society of Naval Architects of Korea. URL: https://doi.org/10.1016/j.ijnaoe.2020.12.002.

Tezdogan, T., Incerik, A., Turan, O., 2015. A numerical investigation of the squat and resistance of ships advancing through a canal using cfd. In: JASNAOE 2015. Vol. 21, pp. 86–101, URL: http://dx.doi.org/10.1007/s00773-015-0334-1.

Tokyo, 2015. 2015: A Workshop on Cfd on Ship Hydrodynamics. URL: https://www.t2015.nmri.go.jp/kcs_gc.html.

Townsin, R., Mosaad, M., 1985. The ittc line - its genesis and correlation allowance. Nav. Archit. E359.

Watanabe, K., 1973. Note to the performance committee. URL: https://ittc.info/media/3267/rpec.pdf.

Wilson, R., Stern, F., Coleman, H., Paterson, E., 2001. Comprehensive approach to verification and validation of cfd simulations—part 2: Application for rans simulation of a cargo/container ship. J. Fluids Eng. 123, 803–810.

Yao, J.X., Liu, Z., Song, X., Su, Y., 2021. Ship maneuvering prediction with hydrodynamic derivatives from rans: Development and application. Ocean Eng. 231, 109036, URL: https://doi.org/10.1016/j.oceaneng.2021.109036.